Received: Added at production | Revised: Added at production | Accepted: Added at production

DOI: xxx/xxxx

ARTICLE TYPE

Hybrid equilibrium element with inter-element interface for the analysis of delamination and crack propagation problems

Francesco Parrinello*

Engineering Department, University of Palermo, Viale delle Scienze, Ed. 8, 90128 Palermo Italy

Correspondence
*Email: francesco.parrinello@unipa.it

Present Address
This is sample for present address text this is sample for present address text

Summary

The present paper proposes a formulation for the analysis of delamination and fracture propagation problems at the inter-element interface, with perfect adhesion at the pre-failure condition and with linear softening at the post-failure regime. The proposed formulation is based on the hybrid equilibrium element (HEE) model, with stress fields which strongly verify the homogeneous equilibrium equations and inter-element equilibrium equations. The HEE can easily model high-order stress fields and can implicitly model the initially rigid behaviour of an extrinsic interface at the element sides. The interface model is defined as a function of the same degrees of freedom of the HEE (generalized stresses) and the pre- and post-failure behaviour of the interface can be modelled without any additional degree of freedom. The proposed formulation is developed for a nine-node triangular hybrid equilibrium element with quadratic stress fields. The paper also proposes an extrinsic cohesive model, rigorously developed in the damage mechanics framework.

KEYWORDS:
Extrinsic Interface, Inter-element fracture, Equilibrium element

1 | INTRODUCTION

The mechanical behaviour of brittle and quasi-brittle materials subjected to severe tensile and shear stresses is characterized by a complex system of irreversible micro-mechanical phenomena such as diffuse damage, micro-cracking and eventually fracture, which can evolve to material failure and as the ultimate state to the collapse of structural elements. Constitutive modelling of the nonlinear behaviour of brittle materials can be approached in the framework of continuum damage mechanics or by the discrete crack model of fracture. The former approach, in order to mantain a well posed formulation and avoid a pathological mesh dependency, imposes a regularization technique such as gradient or non-local formulations [1,2,3], or following a recent trend, phase-field damage models [4,5,6]. In continuum damage mechanics the formation and propagation of the crack pattern is not postulated a priori and is not explicitly modelled. Conversely, discrete crack models are based on explicit modelling of the separation surface within the material and by the kinematic formulation of discontinuous displacement fields. The discrete crack can be modelled as a zero-thickness interface element, the simplest formulation and the natural choice for problems with predefined failure surface. More advanced formulations for crack propagation across a pre-existing finite element mesh are the strong or embedded discontinuity (EFEM) approaches [7,8,9,10] and the eXtended-generalized FEM (XFEM, GFEM) [11,12,13,14]. The XFEM is a powerful numerical formulation enabling crack propagation with an arbitrary path without remeshing; it also simplifies discretization of different bodies joined together along an existing surface, meshing the whole domain with the interface crossing through the elements [15,16]. Comparative analysis between EFEM and XFEM is presented by Oliver et al [17].

Discrete crack models are often combined with Cohesive Zone Models (CZM), which describe the Traction Separation Law (TSL) at the discontinuity surface. The CZMs, initially proposed in the pioneering works of Dugdale[18] and Barenblatt[19], allow us to overcome the mathematical issue of the stress singularity ahead of the crack tip of linear elastic fracture mechanics[20].

The literature is extremely rich in cohesive interface models, and several points of view have been thoroughly investigated, such as the following: isotropic and orthotropic cohesive interface models[21], coupling damage and plasticity[22], different mode I and mode II fracture energies[23,24,25], thermodynamic consistency[26,27,28], with smooth transition from cohesive behaviour to frictional one[29,26], under finite displacement conditions[23,30] etc. The references cited represent a short and largely incomplete review of the interface models available in literature. All the cited models assume as elastic the behaviour in the pre-failure regime, with an active displacement jump between the two edges of the discontinuity surface. Such elastic behaviour allows one to reproduce the initial reversible behaviour of a finite thickness adhesive layer, condensed to a zero thickness interface, or represents the approximation of the penalty method applied to keep together the two connected bodies along the joining surface. Moreover, the penalty methods usually models the closure conditions of a fully debonded interface. The penalty method introduces an additional and artificial compliance which alters the elastic response, and it can produce pathological traction oscillations at the crack tip[31] with incorrect evaluation of the crack advancement condition.

An effective alternative to the penalty method for the modelling of TSL in the pre-failure regime is proposed in Ref.[32], known as the Hybrid Discontinuous Galerkin (DG) method, and it weakly enforces the displacement continuity at the interface by application of Nitsche's method[33]. When the failure condition is reached, the joining condition is released, switching form the DG method to the interface formulation with an extrinsic (initially rigid) TSL. This approach ensures a seamless transition from perfect adhesion to softening behaviour. Nitsche's method, in the form of DG combined with an extrinsic TSL,is also presented in Ref.[34] for modelling of the interfacial cracking between non-matching meshes, in Ref.[35] for debonding between fibre and matrix in composite materials, and in Refs.[36,37] for intergranular degradation and failure in polycrystalline materials, through the boundary element method.

The DG is applied in Ref.[38] for the analysis of interface separation of both the static problem and the dynamic one. The results, compared to the classic interface formulation, show significant differences in the wave speed, due to the additional compliance induced by the penalty method in the interface formulation.

The adhesion condition at the interface for a known crack path is strongly enforced in Ref.[39] through a mixed formulation, based on the augmented Lagrangian method. The interface mixed formulation explicitly models separation displacement and cohesive traction, the latter considered as a Lagrangian variable. The extrinsic rigid-damage TSL is modelled in terms of the cohesive surface energy density and the crack propagation problem is given in terms of minimisation of a Lagrangian functional. The problem of non-differentiability of the cohesive energy at the adhesion condition is circumvented thanks to a specific crack initiation criterion.

The considerable improvement given by the DG method, with respect to the penalty one, is the perfect adhesion, although applied in a weak form, between the two sides of the interface, without the additional degrees of freedom of the mixed formulation[39]. By stark contrast, the intrinsic TSL and penalty method produce imperfect adhesion and artificial compliance, with wave propagation issues.

The advantages afforded by the DG method with extrinsic TSL are fundamental in the formulation proposed in Refs.[40,41], where the dynamic crack propagation on an arbitrary path has been modelled. In Refs.[40,41] the interface elements are inserted at every inter-element boundary and constrained to the adhesion condition by the DG method, as long as the crack initiation condition is not attained. The crack does not propagate across the elements, like in the XFEM, but propagates at the inter-element interfaces. Moreover, in Ref.[41] fracture and fragmentation are numerically simulated in an effective parallel computational framework. The main drawback of such formulations is mesh dependency; however, this problem can be mitigated by mesh refinement. Details of implementation of the DG formulation with CMZs are presented in Ref.[42].

Crack propagation at the inter-element interface is also proposed in Refs.[43,44], with the same formulation as proposed by[39], but with a continuation method in order to overcome the non-differentiability issue of the cohesive energy at the pre-failure condition.

The formulation proposed in the present paper can be posed in the same computational framework as that of the papers cited[32,39,41,44] for delamination and fracture propagation analysis at the inter-element interface, with perfect adhesion at the pre-failure condition and with an extrinsic CZM for the post-failure regime. The novelty of the present paper in the analysis of fracture propagation at the inter-element interface is the use of an equilibrium-based finite element formulation, which provides a solution of the elastic problem with a higher order of stress fields, with respect to the classic displacement-based FEM. Moreover, the accuracy of the stress fields strongly verifies the homogeneous equilibrium equations and inter-element equilibrium

equations[45,46,47,48,49,50,51]. The stress based formulation, with high order stress fields, represents an effective alternative for the analysis of fracture propagation, especially if the fracture initiation criterion is defined as a function of the traction components at the element sides. The proposed formulation is developed for a nine-node triangular hybrid equilibrium element (HEE), with quadratic stress fields, proposed in Ref.[52] for elasto-static analysis of two-dimensional problems. In the present paper, it is shown that the HEE can implicitly reproduces an extrinsic interface at the element sides and, once the fracture activation condition is attained, also the cohesive failure of the interface with rigid-damage behaviour. The interface TSL is defined as a function of the same degrees of freedom of the HEE (generalized stresses) and the pre- and post-failure behaviour of the interface can be modelled without any additional degree of freedom. The paper proposes an extrinsic TSL, developed in the damage mechanics framework with rigorous satisfaction of thermodynamic principles.

The paper is organized as follows: the HEE is developed in Section 2. The HEE with an interface embedded at one element side is proposed in Section 3. The extrinsic TSL with the relevant damage activation condition is presented in Section 4. The interface full debonding condition is analyses in Section 5. The results of the numerical simulations for delamination and crack propagation tests are reported in Section 6 and, finally, closing remarks are given in Section 7.

2 | DYNAMIC AND STATIC EQUILIBRIUM FORMULATIONS

Let us consider an elastic body occupying the closed region Ω. The body is referred to a Cartesian reference system (x, y) and is subjected to body force $\mathbf{b}$ in Ω, traction $\mathbf{t}$ on the free boundary Γ_T and imposed displacement $\overline{\mathbf{u}}$ on the constrained boundary $\Gamma_U = \Gamma \cap \Gamma_T$. The equilibrium formulation belongs to the class of stress-based approaches and the weak form solution of the elasto-static problem is given as the stationary condition of the complementary energy functional

$$\Pi_c = \frac{1}{2}\int_{\Omega} \boldsymbol{\sigma} : \mathbf{D} : \boldsymbol{\sigma}\, d\Omega - \int_{\Gamma_U} \mathbf{n}^T \cdot \boldsymbol{\sigma} \cdot \overline{\mathbf{u}}\, d\Gamma \tag{1}$$

where the stress tensor $\boldsymbol{\sigma}$ is assumed to satisfy the domain and boundary equilibrium equations, $\mathbf{D}$ is the fourth-order elastic compliance tensor and $\mathbf{n}$ is the unit vector normal to the constrained boundary Γ_U.

The static hybrid equilibrium formulation considered in the present paper for the stress-based solution of the elastic two-dimensional problem follows the same reasoning path as proposed in Ref.[52?]. The spatial domain is discretized by a set of N_e non-overlapping triangular subdomains Ω_e, with $\bigcup_{e=1}^{N_e} \Omega_e = \Omega$. The element subdomain boundary $\Gamma^e = \partial\Omega_e$ is composed of three sides Γ_s^e with $s = 1, 2, 3$, each of which can lie at the free boundary $\Gamma_s^e \subset \Gamma_T$, or can lie at the constrained boundary $\Gamma_s^e \subset \Gamma_U$, or can be an internal side between two subdomains $\Gamma_{int} \equiv \partial\Omega e_1 \cap \partial\Omega e_2$, with $e_1 \neq e_2$. The stress fields $\boldsymbol{\sigma}_e$ are independently defined for each finite element and satisfy the equilibrium equation in the element domain ($\mathrm{div}\, \boldsymbol{\sigma}_e + \mathbf{b} = \mathbf{0}$ in Ω_e)

The inter-element equilibrium condition, at all internal sides, and the boundary equilibrium condition at all free boundary sides are imposed by the classical hybrid formulation, for which independent displacement fields $\mathbf{u}_s^e(\mathbf{x})$ are defined for each element side Γ_s^e, and they are assumed as Lagrangian variables in order to mutually connect adjacent elements or to apply traction on the free boundary[48,53,51]. For a triangular finite element discretization, the weak form of the Lagrangian approach gives the following modified total complementary energy functional:

$$\overline{\Pi}_c = \sum_{e=1}^{N_e} \left[\frac{1}{2}\int_{\Omega_e} \boldsymbol{\sigma}^e : \mathbf{D} : \boldsymbol{\sigma}^e\, d\Omega - \sum_{s=1}^{3} \left(\int_{\Gamma_s^e} \mathbf{n}_s^e \cdot \boldsymbol{\sigma}^e \cdot \mathbf{u}_s^e\, d\Gamma - \int_{\Gamma_s^e \cap \Gamma_T} \mathbf{t} \cdot \mathbf{u}_s^e\, d\Gamma \right) \right] \tag{2}$$

with $\mathbf{u}_s^e = \overline{\mathbf{u}}$ on $\Gamma_s^e \cap \Gamma_U$ and $\mathbf{n}_s^e$ the outward normal to side Γ_s^e.

The stationary conditions of the functional $\overline{\Pi}_c$, with respect to the Lagrangian variable $\mathbf{u}$ at the internal side $\Gamma_{int} = \partial\Omega_{e_1} \cap \partial\Omega_{e_2}$ between elements e_1 and e_2, gives

$$\int_{\Gamma_{int}} (\mathbf{n}^{e_1} \cdot \boldsymbol{\sigma}^{e_1} + \mathbf{n}^{e_2} \cdot \boldsymbol{\sigma}^{e_2}) \cdot \delta\mathbf{u}\, d\Gamma = \mathbf{0} \quad \forall \delta\mathbf{u} \tag{3}$$

where the outward normals of the adjacent elements at the inter-element side are $\mathbf{n}^{e_1} = -\mathbf{n}^{e_2}$. Equation (3) provides the weak form of the inter-element equilibrium condition. For a free boundary side $\Gamma_s^e = \partial\Omega_e \cap \Gamma_T$ the stationary condition of the functional

$\overline{\Pi}_c$, with respect to the Lagrangian variable u_i, gives

$$\int_{\Gamma_s^e} (\mathbf{n}^e \cdot \boldsymbol{\sigma}^e - \mathbf{t}) \cdot \delta\mathbf{u} \, d\Gamma = \mathbf{0} \;\; \forall \delta\mathbf{u}, \tag{4}$$

which provides the weak form of the boundary equilibrium condition.

The stationary conditions of the functional $\overline{\Pi}_c$, with respect to the stress tensor $\boldsymbol{\sigma}^e$ on the element Ω_e, gives

$$\int_{\Omega_e} \delta\boldsymbol{\sigma}^e : \mathbf{D} : \boldsymbol{\sigma}^e \, d\Omega - \int_{\partial\Omega_e = \Gamma^e_{s=1,3}} \mathbf{n}_s^e \cdot \delta\boldsymbol{\sigma}^e \cdot \mathbf{u}_s^e \, d\Gamma = 0 \quad \forall \delta\boldsymbol{\sigma}^e / \operatorname{div} \delta\boldsymbol{\sigma}^e = \mathbf{0} \;\text{ in }\; \Omega_e, \tag{5}$$

which gives the principle of complementary virtual work for the triangular domain Ω^e subjected to the imposed displacement $\mathbf{u}_s^e$ (Lagrangian variable) at the boundary sides Γ_s^e (with $s = 1, 3$) and with the virtual stress $\delta\boldsymbol{\sigma}^e$ satisfying domain equilibrium equation for null body forces. Equation (5) provides a weak form of the compatibility condition between elastic strains $\epsilon^e = \mathbf{D} : \boldsymbol{\sigma}^e$ and imposed displacement at the boundary sides.

2.1 | The hybrid equilibrium element

In hybrid equilibrium formulations the finite element is defined by the element stress fields satisfying the domain equilibrium equation (**??**), which does not interpolate nodal degrees of freedom, but is a function of generalized stresses. In the present paper, the hybrid equilibrium element is developed only for two-dimensional membrane problems with a quadratic stress fields.

Let a triangular finite element of domain Ω_e be considered and referred to a local Cartesian reference (x_1, x_2) centred at vertex 1, as shown in Fig. 1. The membrane stress fields are defined by the following quadratic polynomial functions

$$\sigma_1 = a_1 + a_2 x_1 + a_3 x_2 + 2a_4 x_1 x_2 + a_5 x_1^2 + a_6 x_2^2 - b_1 x_1, \tag{6}$$

$$\sigma_2 = a_7 + a_8 x_1 + a_9 x_2 + 2a_{10} x_1 x_2 + a_{11} x_1^2 + a_5 x_2^2 - b_2 x_2, \tag{7}$$

$$\tau_{12} = a_{12} - a_9 x_1 - a_2 x_2 - 2a_5 x_1 x_2 - a_{10} x_1^2 - a_4 x_2^2, \tag{8}$$

where, b_1 and b_2 are components of body force, and terms $a_1, \ldots, a_{12}$ are generalized stress variables. The stress fields of Eqs.(6-8) implicitly satisfy equilibrium Equation (**??**) and can be represented in the following Voigt notation

$$\boldsymbol{\sigma} = \mathbf{S} \cdot \mathbf{a} + \boldsymbol{\sigma}_0 \tag{9}$$

where $\mathbf{a}$ collects all generalized stress variables and $\boldsymbol{\sigma}_0 = \left[-b_1 x_1, -b_2 x_2, 0\right]^T$ is the particular solution of Eq.(**??**), due to a uniform body load, and $\boldsymbol{\sigma} = \left[\sigma_1, \sigma_2, \tau_{12}\right]^T$.

The inter-element and boundary equilibrium conditions are imposed by a Lagrangian approach, and an independent displacement field, for each element side, is considered as a Lagrangian variable. For the proposed HEE, with the quadratic stress fields in Eq.(6-8), a quadratic polynomial displacement field, with three independent nodes for every element side, allows the proposed formulation to strongly verify the inter-element equilibrium condition, with codiffusive stresses $\boldsymbol{\sigma}^{e_1}$ and $\boldsymbol{\sigma}^{e_2}$ through the inter-element side $\Gamma_{int} = \partial\Omega_{e_1} \cap \partial\Omega_{e_2}$. The quadratic HEE is governed by nine nodes, with two geometrically coincident nodes for each vertex, as represented in Fig.(1). Displacement fields are independently defined at each element side and they are generally discontinuous. In fact, in the proposed stress-based approach, equilibrium conditions are strongly satisfied, whereas displacement continuity cannot be imposed. By contrast, in displacement-based formulations, displacement continuity is imposed but tractions at sides are discontinuous between adjacent elements. Similarly, in the DG approach the displacement continuity is only weakly enforced at all the interface between adjacent elements. The geometry and displacement components of the element sides Γ_s^e with $s = 1, 2, 3$ are modelled by a classic isoparametric mapping

$$x_i^s(\xi) = \sum_{r=1}^{3} N_r(\xi) \, X_i^m, \tag{10}$$

$$u_i^s(\xi) = \sum_{r=1}^{3} N_r(\xi) \, U_i^m, \tag{11}$$

where the node number is $m = 3(s-1) + r$; $N_r(\xi)$ is the r^{th} quadratic shape function in the natural coordinate $-1 \le \xi \le 1$; U_i^m and X_i^m respectively are the displacement component and the Cartesian coordinate of node m. Eq.(11) can be rewritten in

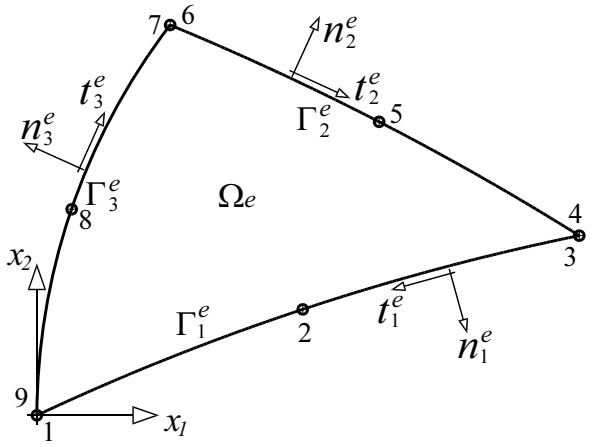

FIGURE 1 Nine-node hybrid triangular finite element.

matrix notation as

$$\boldsymbol{u}_s^e(\xi) = \mathbf{N}(\xi) \cdot \mathbf{u}_s^e, \tag{12}$$

where $\mathbf{N}$ collects the shape functions and $\mathbf{u}_s^e$ collects the kinematic degrees of freedom of side Γ_s^e.

The complementary energy functional $\overline{\Pi}_c$ can be written in the discretized form as

$$\overline{\Pi}_c = \sum_{e=1}^{n_e} \left[\frac{1}{2} \mathbf{a}_e^T \mathbf{C}_e \mathbf{a}_e - \mathbf{a}_e^T \mathbf{H}_e \mathbf{u}_e + \mathbf{T}_e^T \mathbf{u}_e \right], \tag{13}$$

where

$$\mathbf{C}_e = \int_{\Omega_e} \mathbf{S}_e^T \mathbf{D}\, \mathbf{S}_e d\Omega, \tag{14}$$

$$\mathbf{H}_e = \left[\mathbf{h}_1^e, \mathbf{h}_2^e, \mathbf{h}_3^e \right], \tag{15}$$

$$\mathbf{h}_s^e = \int_{\Gamma_s^e} \mathbf{S}_e^T \mathbf{n}_s^e\, \mathbf{N} d\Gamma, \tag{16}$$

$$\mathbf{T}_e = \left[\mathbf{t}_1^e, \mathbf{t}_2^e, \mathbf{t}_3^e \right], \tag{17}$$

$$\mathbf{t}_s^e = \int_{\Gamma_s^e \cap \Gamma_T} \mathbf{N}^T t d\Gamma, \tag{18}$$

$$\mathbf{u}_e = \left[\mathbf{u}_1^e, \mathbf{u}_2^e, \mathbf{u}_3^e \right], \tag{19}$$

$$\mathbf{n}_s^e = \begin{bmatrix} n_{s1}^e & 0 \\ 0 & n_{s2}^e \\ n_{s2}^e & n_{s1}^e \end{bmatrix}. \tag{20}$$

The degrees of freedom of fixed boundaries $\Gamma_s^e \subset \Gamma_U$ are constrained, with assigned value $\overline{\mathbf{u}}$. The stationary condition of function $\overline{\Pi}_c$ in Eq.(13) with respect to the generalized stress vector $\mathbf{a}_e$ gives the following element equation of the discretized hybrid equilibrium formulation

$$\frac{\partial \overline{\Pi}_c}{\partial \mathbf{a}_e} = \mathbf{C}_e \mathbf{a}_e - \mathbf{H}_e \mathbf{u}_e = \mathbf{C}_e \mathbf{a}_e - \mathbf{h}_1^e \mathbf{u}_1^e - \mathbf{h}_2^e \mathbf{u}_2^e - \mathbf{h}_3^e \mathbf{u}_3^e = \mathbf{0}, \tag{21}$$

which states the relationship between nodal displacement and generalized stress variables at the element level. The element nodal force vector can also be written as $\mathbf{q}_e = \mathbf{H}_e^T \mathbf{a}_e$ and the equation of the single hybrid equilibrium element is

$$\begin{bmatrix} \mathbf{C}_e & -\mathbf{H}_e \\ -\mathbf{H}_e^T & \mathbf{0} \end{bmatrix} \begin{bmatrix} \mathbf{a}_e \\ \mathbf{u}_e \end{bmatrix} = \begin{bmatrix} \mathbf{0} \\ -\mathbf{q}_e \end{bmatrix} \tag{22}$$

where the compliance matrix $\mathbf{C}_e$ is symmetric, positive definite and is not singular, so that it can be inverted and the generalized stress $\mathbf{a}_e$ can be condensed out at the element level; that is, mathematically

$$\mathbf{a}_e = \mathbf{C}_e{}^{-1}\mathbf{H}_e\mathbf{u}_e \tag{23}$$

$$\mathbf{q}_e = \mathbf{H}_e^T\mathbf{C}_e{}^{-1}\mathbf{H}_e\mathbf{u}_e = \mathbf{K}_e\mathbf{u}_e \tag{24}$$

where the matrix $\mathbf{K}_e = \mathbf{H}_e^T\mathbf{C}_e{}^{-1}\mathbf{H}_e$ is the element stiffness matrix and the HEE can be implemented in a classic displacement-based finite element code. The drawback of the HEE is the possible presence of well-known spurious kinematic modes, which must be controlled or restrained by means of different available strategies[52,53,54,55].

3 | HEE WITH INTERFACE EMBEDDED

The hybrid equilibrium element, with its property of independent displacement fields for each side, is particularly suitable for modelling of decohesion along an element side, without any additional degree of freedom.

3.1 | Elastic interface

In order to simplify the formulation, an elastic interface Γ_0 is initially considered inside the two-dimensional elastic domain Ω, which is divided into a positive part and a negative one, respectively Ω_+ and Ω_-, as represented in Fig.2a. The elastic behaviour of the connecting surface Γ_0 is modelled by a linear relationship between traction components $\mathbf{s} = \boldsymbol{\sigma}^-\mathbf{n} = -\boldsymbol{\sigma}^+\mathbf{n}$ and the separation displacement $[\![\mathbf{u}]\!] = \mathbf{u}^+ - \mathbf{u}^-$

$$[\![\mathbf{u}]\!] = \mathbf{A}^{el}\mathbf{s}, \tag{25}$$

where $\boldsymbol{\sigma}^+$ and $\mathbf{u}^+$ are respectively the stress and displacement of points $\mathbf{x} \in \Omega_+ \cap \Gamma_0$, $\boldsymbol{\sigma}^-$ and $\mathbf{u}^-$ are respectively the stress and displacement of points $\mathbf{x} \in \Omega_- \cap \Gamma_0$ and matrix $\mathbf{A}^{el}$ is the interface compliance diagonal matrix.

The elastic interface introduces an additional elastic strain energy contribution in the complementary energy functional in Eq.(2) and its spatial discretized form, in Voigt notation, is given as

$$\overline{\Pi}_c = \sum_{e=1}^{N_e}\left[\frac{1}{2}\int_{\Omega_e}\boldsymbol{\sigma}_e^T\mathbf{D}\,\boldsymbol{\sigma}_e\,d\Omega + \frac{1}{2}\int_{\Gamma^e\cap\Gamma_0}\mathbf{s}^T\mathbf{A}^{el}\mathbf{s}\,d\Gamma + \right.$$
$$\left. - \sum_{s=1}^{3}\left(\int_{\Gamma_s^e}\mathbf{n}_s^{eT}\boldsymbol{\sigma}_e^T\mathbf{u}_s^e\,d\Gamma - \int_{\Gamma_s^e\cap\Gamma_T}\mathbf{t}^T\mathbf{u}_s^e\,d\Gamma\right)\right] \tag{26}$$

The interface is embedded at the element side and the interface traction can be modelled as a function of the same vector $\mathbf{a}_e$ of generalized stress variables as adopted for the stress functions in Eqs.(6-9) of the HEE formulation [1] . For an interface embedded at the side Γ_1^e (and for null body force $\mathbf{b} = \mathbf{0}$) traction can be defined in equilibrium with element stress fields as

$$\boldsymbol{s}(\mathbf{x}) = \boldsymbol{\sigma}^T\mathbf{n}_1^e = \mathbf{a}_e^T\mathbf{S}^T(\mathbf{x})\,\mathbf{n}_1^e \quad \text{with} \quad x \in \Gamma_1^e \subset \Gamma_0. \tag{27}$$

where $\mathbf{n}_1^e$ is the normal unit vector at the element side Γ_1^e (outward from the finite element). For the proposed HEE formulation with embedded elastic interface at element sides the complementary energy functional in Eq.(26) can be written in the following discretized form

$$\overline{\Pi}_c = \sum_{e=1}^{n_e}\left[\frac{1}{2}\mathbf{a}_e^T\left(\mathbf{C}_e + \mathbf{C}_e^\Gamma\right)\mathbf{a}_e - \mathbf{a}_e^T\mathbf{H}_e\mathbf{u}_e + \mathbf{T}_e^T\mathbf{u}_e\right], \tag{28}$$

where

$$\mathbf{C}_e^\Gamma = \int_{\Gamma_1^e\subset\Gamma_0}\mathbf{S}_e^T\mathbf{n}_1^e\,\mathbf{A}^{el}\mathbf{n}_1^{eT}\mathbf{S}_e d\Gamma. \tag{29}$$

[1]For a HEE with embedded elastic interface at the boundary sides, the stationary condition of functional $\overline{\Pi}_c$ with respect to stress $\boldsymbol{\sigma}_e$ is defined as: $\int_{\Omega_e}\delta\boldsymbol{\sigma}_e^T\mathbf{D}\boldsymbol{\sigma}^e\,d\Omega - \int_{\partial\Omega_e}\mathbf{n}_s^e\delta\boldsymbol{\sigma}^e\left(\mathbf{u}_s^e - [\![\mathbf{u}]\!]\right)d\Gamma = 0 \quad \forall\delta\boldsymbol{\sigma}^e \,/\, \operatorname{div}\delta\boldsymbol{\sigma}^e = \mathbf{0}$ in Ω_e. This equation provides the principle of complementary virtual work for the element domain Ω_e subjected to the imposed displacement $\mathbf{u}_s^e$ (Lagrangian variable) and with the elastic separation displacement $[\![\mathbf{u}]\!] = \mathbf{A}^{el}\boldsymbol{\sigma}^e\mathbf{n}_s^e$ at the boundary sides (see Fig.3), which gives a weak form of the compatibility condition between elastic strains $\epsilon^e = \mathbf{D} : \boldsymbol{\sigma}^e$ and imposed displacement $\mathbf{u}_s^e - [\![\mathbf{u}]\!]$ at the boundary sides.

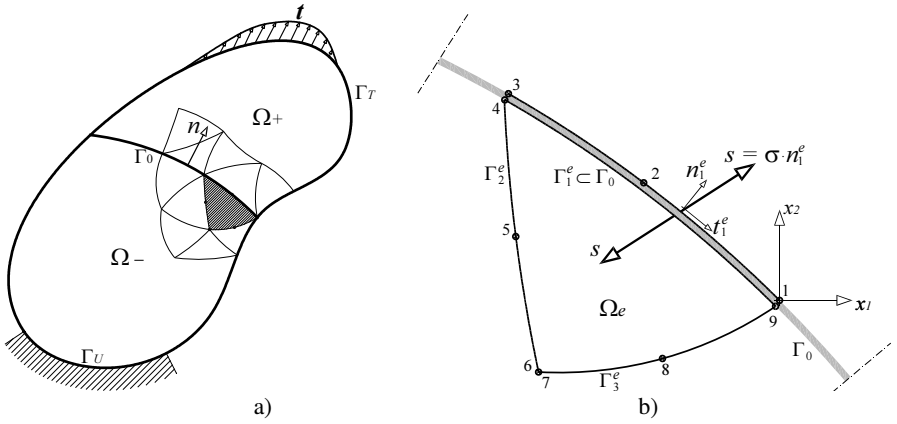

FIGURE 2 a) The elastic domains Ω_+ and Ω_- joined by the elastic interface Γ_0; b) Quadratic hybrid equilibrium element Ω_e with an embedded elastic interface at side Γ_1^e.

is the additional compliance matrix due to the embedded elastic interface. The embedded elastic interface at side Γ_1^e modifies the equation of the single HEE, defined in Eq.(22), with the additional interface compliance matrix $\mathbf{C}_e^\Gamma$ and Eq.(22) becomes

$$\begin{bmatrix} \mathbf{C}_e + \mathbf{C}_e^\Gamma & -\mathbf{H}_e \\ -\mathbf{H}_e^T & \mathbf{0} \end{bmatrix} \begin{bmatrix} \mathbf{a}_e \\ \mathbf{u}_e \end{bmatrix} = \begin{bmatrix} \mathbf{0} \\ -\mathbf{q}_e \end{bmatrix} \tag{30}$$

and the generalized stress vector and the nodal force vector are given as

$$\mathbf{a}_e = \left(\mathbf{C}_e + \mathbf{C}_e^\Gamma\right)^{-1} \mathbf{H}_e \mathbf{u}_e \tag{31}$$

$$\mathbf{q}_e = \mathbf{H}_e^T \left(\mathbf{C}_e + \mathbf{C}_e^\Gamma\right)^{-1} \mathbf{H}_e \mathbf{u}_e = \mathbf{K}_e \mathbf{u}_e, \tag{32}$$

where the matrix $\mathbf{K}_e = \mathbf{H}_e^T \left(\mathbf{C}_e + \mathbf{C}_e^\Gamma\right)^{-1} \mathbf{H}_e$ is the stiffness matrix of the HEE with embedded elastic interface.

In the proposed formulation the elastic interface can be embedded at one or more sides of an hybrid equilibrium element without any additional degrees of freedom, simply considering the additional interface compliance matrix $\mathbf{C}_e^\Gamma$ defined in Eq.(29).

4 | HEE WITH EMBEDDED EXTRINSIC INTERFACE

The previous paragraph shows that the introduction of an embedded elastic interface at the element side of an HEE is quite a simple problem. In the present section, it is shown that the HEE formulation with embedded interface is also particularly effective for modelling an extrinsic interface, which imposes null separation displacement between the positive and negative edges of the interface, until the initial damage activation condition is attained. The extrinsic interface with a rigid-damage cohesive zone model (CZM) has been applied by the use of a discontinuous Galerkin method in Refs.[32,41,42,44] for numerical analysis of delamination phenomena and for analysis of crack propagation. The discontinuous Galerkin method is also proposed in Ref.[34] for interfacial cracking with extrinsic interface combined with non-matching discretization of the domains.

In the present paper the rigid-damage CZM is developed in the rigorous thermodynamic framework of damage mechanics and the model is based on the following Helmholtz free energy function, defined for a unit of interface surface,

$$\Psi = \frac{1}{2} \frac{1-\omega}{\omega} [\![\boldsymbol{u}]\!]^T \mathbf{k}^{el} [\![\boldsymbol{u}]\!] + \Psi_{in}(\xi) \tag{33}$$

where $0 \leq \omega \leq 1$ is the damage variable; $\mathbf{k}^{el}$ is the interface elastic matrix, inverse of compliance matrix $\mathbf{A}^{el}$ defined in Eq.(25); and $\Psi_{in}(\xi)$ is the internal energy, a function of the internal variable ξ. In the classic Coleman-Noll procedure the conjugated

variable can be derived as

$$Y := -\frac{\partial \Psi}{\partial \omega} = \frac{1}{2\omega^2} [\![\boldsymbol{u}]\!]^T \mathbf{k}^{el} [\![\boldsymbol{u}]\!] \tag{34}$$

$$\mathbf{s} := \frac{\partial \Psi}{\partial [\![\boldsymbol{u}]\!]} = \frac{1-\omega}{\omega} \mathbf{k}^{el} [\![\boldsymbol{u}]\!] \tag{35}$$

$$\chi(\xi) := -\frac{d\Psi}{d\xi} = -\frac{\partial \Psi_{in}}{\partial \xi} \tag{36}$$

where Y is the energy release rate, $\mathbf{s}$ is the interface traction and $\chi(\xi)$ is the internal static variable, which governs the interface softening behaviour.

4.1 | Damage activation condition

In the framework of damage mechanics, a thermodynamic consistent formulation analyses the damage activation and evolution as a function of its conjugated variable Y. The damage activation function is defined as

$$\phi_d(Y, \xi) = Y - Y_0 - \chi(\xi) \leq 0 \tag{37}$$

where Y_0 is the threshold for the first damage activation, for which the energy release rate Y in Eq.(34) is in an indeterminate form. In deed, for a perfectly bonded interface, both the damage ω and the separation displacement $[\![\mathbf{u}]\!]$ are identically zero. This difficulty can be overcome if the energy release rate Y is written as a function of the traction instead of the displacement jump by the substitution of Eq.(35) in Eq.(34), that is

$$Y = \frac{1}{2} \frac{1}{(1-\omega)^2} \boldsymbol{s}^T \mathbf{A}^{el} \boldsymbol{s} \tag{38}$$

and at the perfect bonding condition ($\omega = 0$) the energy release rate assumes positive real values.

The proposed CZM is isotropic and produces the same response in the pure opening condition, in the pure sliding one and for all the mixed mode debonding conditions. Moreover, the two modes are fully coupled in the CZM for the dependence of the damage activation condition in Eq.37 on the energy release rate Y, which is defined in Eq.34 in terms of the two separation displacement components (normal and tangential) and in Eq.38 in terms of the traction components. The model could be also extended to a more general formulation, in order to account for different response in pure modes, by an extrinsic formulation of the non-associative damage model proposed by the author in Ref.[25]. The interface elastic stiffness matrix and its inverse are diagonal and defined as $\mathbf{k}^{el} = k_0 \mathbf{I}$ and $A_{ij}^{el} = \mathbf{I}/k_0$ with $\mathbf{I}$ being the identity matrix and k_0 a stiffness parameter. The isotropic model produces the traction vector aligned with the separation displacement vector, as represented in Fig.3 for an extrinsic interface embedded at side $\Gamma_1^{e1} = \partial\Omega_{e1} \cap \Gamma_0$ of the element Ω_{e1}.

The energy release rate threshold is defined as

$$Y_0 = \frac{s_0^2}{2k_0} \tag{39}$$

where s_0 is the interface strength. The interface CZM is fully defined by the following functions of the internal energy and the relevant internal variable law

$$\psi_i(\xi) = Y_0 \left(\frac{u_f^2/(u_f - u_e)}{u_f(1-\xi) + u_e\xi} - \xi \right) \tag{40}$$

$$\chi(\xi) = Y_0 \left[\left(\frac{u_f}{u_f(1-\xi) + u_e\xi} \right)^2 - 1 \right] \tag{41}$$

where u_f is the separation displacement at the fully debonding condition and $u_e = s_0/k_0$. The evolution of damage and of the internal kinematic variable is governed by the following associative flow rules and loading-unloading conditions

$$\dot{\omega} := \frac{\partial \phi}{\partial Y} \dot{\lambda}_d = \dot{\lambda}_d \tag{42}$$

$$\dot{\xi} := \frac{\partial \phi}{\partial \chi} \dot{\lambda}_d = \dot{\lambda}_d \tag{43}$$

$$\dot{\lambda}_d \geq 0, \quad \phi \dot{\lambda}_d = 0, \quad \dot{\phi} \dot{\lambda}_d = 0. \tag{44}$$

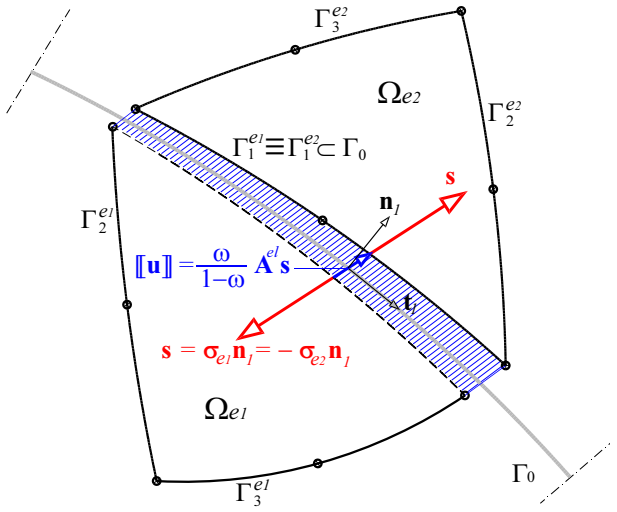

FIGURE 3 Extrinsic interface embedded at side $\Gamma_1^{e1} = \partial\Omega_{e1} \cap \Gamma_0$ with isotropic traction separation law.

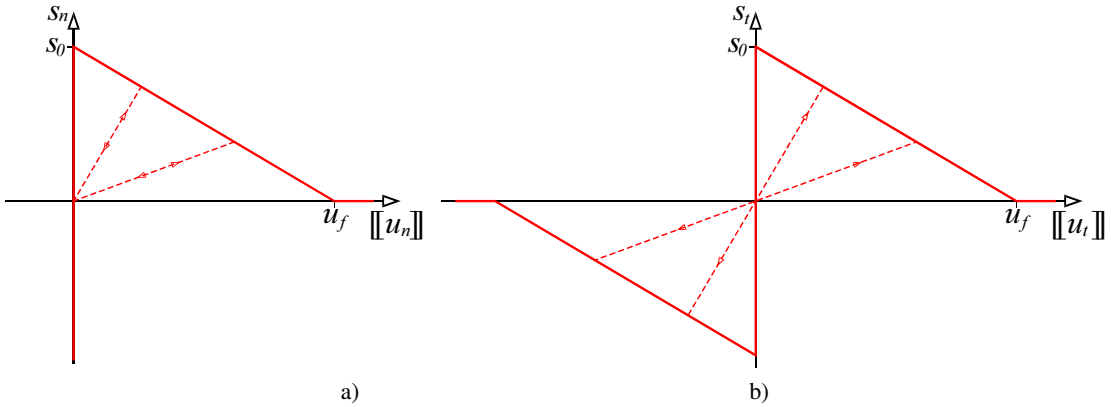

FIGURE 4 Bilinear response of the proposed extrinsic interface model with linear unloading-reloading conditions: a) pure opening mode with unlimited strength in compressive normal traction; b) pure sliding mode.

The proposed extrinsic CZM, with the static variable evolution law in Eq.(41) and the associative flow rules, produces the bilinear traction separation law represented in Figures 4a,b, with a straight unloading-reloading branch and unlimited strength in compressive normal traction.

The interface constitutive law and the relevant Helmholtz free energy in Eq.(33) could be defined in terms of traction. However, the displacement based formulation should be introduced in order to govern the full debonding condition, where the energy release rate in Eq.(38) would be an indeterminate form and the damage activation condition could not be evaluated.

4.2 | Elastic loading step

A hybrid equilibrium element of domain Ω_e and boundary $\Gamma^e = \partial\Omega_e$, with embedded rigid-damage interface at the side $\Gamma_1^e \subset \Gamma_0$, behaves elastically if the damage activation condition in Eq.(37) is negative at all the points of the interface, that is mathematically

$$\phi(\mathbf{x}) < 0 \quad \text{for} \quad \mathbf{x} \in \Gamma_1^e. \tag{45}$$

The elastic behaviour of the interface is modelled by the traction separation law in Eq.(35) with a constant value of the damage variable; the additional interface compliance matrix in Eq.(29) assumes the following form

$$\mathbf{C}_e^{\Gamma} = \int_{\Gamma_1^e \subset \Gamma_0} \frac{\omega}{1-\omega} \mathbf{S}_e^T \mathbf{n}_1^e \, \mathbf{A}^{el} \mathbf{n}_1^{eT} \mathbf{S}_e d\Gamma, \tag{46}$$

and the solution of a loading step with embedded rigid-damage interface can be performed using the element Equation (30) with the additional compliance matrix in Eq.(46). Moreover, for a fully bonded interface ($\omega(\mathbf{x}) = 0$ for $\mathbf{x} \in \Gamma_1^e$) the additional compliance matrix is null $\left(\mathbf{C}_e^{\Gamma} = \mathbf{0}\right)$. As a clear consequence, the full bonded condition of the rigid-damage embedded interface produces a null additional compliance interface matrix, and the behaviour of an HEE with a full bonded extrinsic interface, embedded at an element side, is modelled by an ordinary hybrid equilibrium element. Moreover, it follows that a full bonded extrinsic interface can be implicitly considered embedded at every element side, and explicitly modelled only when the damage activation condition in Eq.(37) is attained. So the additional interface compliance matrix in Eq.(46) has to be considered in Eq.(30), without activation of specific degrees of freedom.

By contrast, in the classic displacement-based finite element formulation, the initial rigid behaviour of the interface can only be applied using a specific numerical formulation, such as the discontinuous Galerkin method. On the other hand, the fully debonded condition is a trivial problem in displacement-based formulation, whereas it requires a specific numerical resolution strategy for the proposed hybrid equilibrium formulation, which will now be described.

4.3 | Damaging loading step

The solution of a loading step involving damage increments requires a specific numerical treatment. The fact is that the solution of such problem cannot be solved at the single Gauss point level, as is classically done in displacement based formulation. Actually, it has to be solved for the whole element with the embedded interface. The HEE with the extrinsic interface embedded at the element side can be considered as a substructure subjected to the imposed displacements at the element sides; its nonlinear response verifies the equilibrium equations in the element domain Ω_e and the consistency condition at the embedded interface. Moreover, the interface tractions are in equilibrium with the stress fields of the adjacent triangular element and are defined as functions of the same generalized stress variables collected in the vector $\mathbf{a}_e$. Hence increment of damage to a single Gauss point of the embedded interface modifies the interface traction, and as a consequence it also modifies the elastic solution of the HEE, the interface tractions at the other Gauss points and the relevant consistency condition.

Let an HEE with embedded extrinsic interface at side Γ_1^e be considered, with a given displacement vector $\mathbf{u}_e$ and generalized stress $\mathbf{a}_e$ (solution of Eq.(31)). The tractions and displacement jumps at the N_G Gauss points ($\mathbf{x}_I \in \Gamma_1^e$ with $1 \le I \le N_G$) of the embedded interface respectively are $\mathbf{s}\left(\mathbf{x}_I\right) = \mathbf{a}_e^T \mathbf{S}^T\left(\mathbf{x}_I\right) \mathbf{n}_1^e$ and $\left[\!\left[\mathbf{u}\left(\mathbf{x}_I\right)\right]\!\right] = \mathbf{A}^{el}\mathbf{s}\left(\mathbf{x}_I\right)$.

If the trial damage consistency condition in Eq.(37) is violated in one or more Gauss points, the solution of the non-linear problem is given in terms of a set of non-negative damage increments $\Delta\boldsymbol{\omega}$ such that the updated generalized stress $\mathbf{a}_e = -\left(\mathbf{C}_e + \mathbf{C}_e^{\Gamma}(\Delta\boldsymbol{\omega})\right)^{-1} \mathbf{H}_e \mathbf{u}_e$ produces interface tractions and interface displacement jumps which satisfy the damage consistency condition at all the Gauss points. Hereafter the index e of the element and the index 1 of the side will be omitted and the additional interface compliance matrix can be written by the following Gauss numerical integration

$$\mathbf{C}^{\Gamma}(\Delta\boldsymbol{\omega}) = \sum_{I=1}^{N_G} \frac{\omega_I + \Delta\omega_I}{1-\omega_I-\Delta\omega_I} \mathbf{S}_I^T \mathbf{n}_I \, \mathbf{A}^{el} \mathbf{n}_I{}^T \mathbf{S}_I W_I, \tag{47}$$

where N_G is the number of Gauss integration points; $\Delta\boldsymbol{\omega}$ is the vector collecting the N_G damage increments; $W_I = w_I J_I$ is the product of the Gauss point weight w_I times the jacobian of the isoparametric interface mapping J_I. The damage increments must satisfy the damage activation condition, the flow rules and the loading-unloading conditions, which can be written at the Gauss points in the following form:

$$\phi_I = Y_I - Y_0 - \chi\left(\xi_I + \Delta\xi_I\right) \leq 0 \tag{48}$$

$$Y_I = \frac{1}{2}\frac{1}{\left(1-\omega_I-\Delta\omega_I\right)^2}\mathbf{s}_I^T\mathbf{A}_I^{el}\mathbf{s}_I \tag{49}$$

$$\Delta\omega_I = \Delta\xi_I \geq 0 \tag{50}$$

$$\phi_I\Delta\omega_I = 0 \tag{51}$$

$$\Delta\phi_I\Delta\omega_I = 0 \;\; I = 1,\ldots,N_G. \tag{52}$$

If the trial damage activation condition is violated in a number M_G (with $1 \leq M_G \leq N_G$) of Gauss points ($\phi_J > 0$, with $J = 1,..,M_G$) the solution of the nonlinear problem is defined by the set of unknown damage increments

$$\Delta\bar{\boldsymbol{\omega}} = \left[\omega_1,\ldots,\omega_{M_G}\right]^T \tag{53}$$

and the generalized stress vector $\bar{\mathbf{a}}$ which verify as zero the consistency condition of the M_G violated Gauss points and the HEE equation, written in the following residual form

$$\mathbf{R}\left(\bar{\mathbf{a}},\Delta\bar{\boldsymbol{\omega}}\right) = \left[\mathbf{C}+\mathbf{C}^{\Gamma}\left(\Delta\bar{\boldsymbol{\omega}}\right)\right]\bar{\mathbf{a}} - \mathbf{H}\mathbf{u} = \mathbf{0} \tag{54}$$

$$\boldsymbol{\Phi}\left(\bar{\mathbf{a}},\Delta\bar{\boldsymbol{\omega}}\right) = \left[\phi_1 W_1,\ldots,\phi_{M_G}W_{M_G}\right]^T = \mathbf{0} \tag{55}$$

where the terms W_I have been introduced for symmetry reasons. The solution of this nonlinar problem can be achieved by a classic iterative Newton-Rapson (NR) approach and Equations (54) and (55) can be written as

$$\begin{aligned}\mathbf{R}^{i+1} &\cong \mathbf{R}^i + \frac{\partial\mathbf{R}}{\partial\mathbf{a}}d\mathbf{a} + \frac{\partial\mathbf{R}}{\partial\Delta\bar{\boldsymbol{\omega}}}d\Delta\bar{\boldsymbol{\omega}} = \\ &= \mathbf{R}^i + \left[\mathbf{C}+\mathbf{C}^{\Gamma}\right]d\mathbf{a} + \mathbf{K}_{\omega}d\Delta\bar{\boldsymbol{\omega}} = \mathbf{0}\end{aligned} \tag{56}$$

$$\boldsymbol{\Phi}^{i+1} \cong \boldsymbol{\Phi}^i + \frac{\partial\boldsymbol{\Phi}}{\partial\mathbf{a}}d\mathbf{a} + \frac{\partial\boldsymbol{\Phi}}{\partial\Delta\bar{\boldsymbol{\omega}}}d\Delta\bar{\boldsymbol{\omega}} = \mathbf{0} \tag{57}$$

where $\mathbf{R}^i = \mathbf{0}$, $\frac{\partial\mathbf{R}}{\partial\mathbf{a}} = \mathbf{C}+\mathbf{C}^{\Gamma}$, $\mathbf{K}_{\omega} = \frac{\partial\mathbf{R}}{\partial\Delta\bar{\boldsymbol{\omega}}} = \left[\mathbf{K}_{\omega_1},\ldots,\mathbf{K}_{\omega_{MG}}\right]$ with

$$\mathbf{K}_{\omega_J} := \frac{\partial\mathbf{R}}{\partial\Delta\omega_J} = \frac{\partial\mathbf{C}^{\Gamma}}{\partial\Delta\omega_J}\mathbf{a} = \frac{1}{\left(1-\omega_J-\Delta\omega_J\right)^2}\mathbf{S}_J^T\mathbf{n}_J\,\mathbf{A}_J^{el}\mathbf{s}_J J_J W_J, \tag{58}$$

Moreover, the derivatives of the vector of the violated consistency conditions are

$$\frac{\partial\Phi_J}{\partial\mathbf{a}} = \mathbf{K}_{\omega_J}^T = \frac{1}{\left(1-\omega_J-\Delta\omega_J\right)^2}\mathbf{s}_J^T\mathbf{A}_J^{el}\mathbf{n}_I^T\mathbf{S}_I W_J \tag{59}$$

$$\begin{aligned}K_{\phi_{IJ}} := \frac{\partial\Phi_I}{\partial\Delta\omega_J} = \Bigg[&\frac{1}{\left(1-\omega_I-\Delta\omega_I\right)^3}\mathbf{s}_I^T\mathbf{A}_I^{el}\mathbf{s}_I + \\ &-\frac{2Y_0u_f^2\left(u_f-u_e\right)}{\left[u_f\left(1-\omega_I-\Delta\omega_I\right)+u_e\left(\omega_I+\Delta\omega_I\right)\right]^3}\Bigg]\delta_{IJ}\end{aligned} \tag{60}$$

with $I,J = 1,\ldots,M_G$ and δ_{IJ} the Kronecker delta. The set of non linear Equations (56-57), with the position assumed in Eqs.(58-60), can be rewritten in the following matrix notation

$$\begin{bmatrix}\mathbf{C}+\mathbf{C}^{\Gamma} & \mathbf{K}_{\omega}\\ \mathbf{K}_{\omega}^T & \mathbf{K}_{\phi}\end{bmatrix}\begin{bmatrix}d\mathbf{a}\\ d\Delta\bar{\boldsymbol{\omega}}\end{bmatrix} = \begin{bmatrix}\mathbf{0}\\ -\boldsymbol{\Phi}^i\end{bmatrix} \tag{61}$$

and the solution of the single Newton-Rapson interation is

$$d\Delta\bar{\boldsymbol{\omega}} = \left[\mathbf{K}_{\omega}^T\left(\mathbf{C}+\mathbf{C}^{\Gamma}+\right)^{-1}\mathbf{K}_{\omega} - \mathbf{K}_{\phi}\right]^{-1}\boldsymbol{\Phi}^i \tag{62}$$

The damage increments can be updated by $\Delta\bar{\boldsymbol{\omega}}^{i+1} = \Delta\bar{\boldsymbol{\omega}}^{i} + d\Delta\bar{\boldsymbol{\omega}}$, whereas the updated generalized stresses are directly evaluated as

$$\bar{\mathbf{a}}^{i+1} = -\left(\mathbf{C} + \mathbf{C}^{\Gamma}\left(\Delta\bar{\boldsymbol{\omega}}^{i+1}\right)\right)^{-1}\mathbf{H}\mathbf{u}, \tag{63}$$

with a quadratic convergence of the proposed iterative formulation. In the Newton-Rapson iterative procedure the set of active Gauss points can change: an active point can assume an elastic behaviour with a negative activation function and *vice versa*. Hence the set of violated consistency conditions collected in Eq.(55) has to be adapted accordingly.

Remark 1. The term $K_{\phi_{IJ}}$ defined in Eq.(60) represents the variation of function Φ_I due to the increment of damage $d\Delta\omega_J$ (for fixed traction $\mathbf{s}_I$). For a positive value of the damage activation function ($\phi_I > 0$), this contribution produces negative damage increment, which is incorrect because of the irreversible nature of the damage variable. Hence at the first iterations, the term $K_{\phi_{IJ}}$ has be neglected in Eq.(60) for correct convergence. Otherwise, the NR problem could converge to a solution with negative damage increments.

The convergence of the nonlinear consistency condition problem in Eqs.(56, 57) is quite effective as can be observed from the following numerical example, which reproduces the pure tensile test represented in Fig.5a of a specimen subjected to a uniform horizontal displacement at the right side (nodes 25, 26, 27). Constrained degrees of freedom (at node 1, 2, 3) are marked in red and the extrinsic interface Γ_0 is embedded at one side of element 4, of nodes 13, 14, 15. The spurious kinematic mode at the external corner of element 3 is restrained by the approach proposed in Ref.[52], that is by a rigid constrain between vertical degrees of freedom of nodes 18 and 25 in Fig.5a. The two-dimensional problem is performed under plane stress condition with elastic constitutive moduli $E = 10000N/mm^2$, $\nu = 0.25$ and the interface is defined with fracture energy $G_I = 1N/mm$ and tensile strength $s_0 = 2N/mm^2$. The pure tensile test produces the bilinear response depicted in Fig.5b in terms of imposed displacement u_x and horizontal force F_x.

After the first damage activation, for $u_x = 0.04mm$, the hybrid equilibrium finite element problem becomes nonlinear and the convergence graphic of the relevant iterative Newton-Rapson (NR) method, for the loading step of imposed displacement $u_x = 0.06mm$, is plotted in the Fig.6a in terms of energy deformation ratio E_i/E_1 and in terms of residual norm ratio R_i/R_1, between the current iteration and the first one.

The inner NR iterative approach defined in Eqs.(56-57) has to be solved for the HEE with embedded interface (element 4), and for each NR iteration of the overall nonlinear loading step. The convergence diagrams of the inner NR approach are plotted in Figures 7a,b, for the first iteration (FE NR iter. 1) and for the last iteration (FE NR iter. 8) of the loading step of imposed displacement $u_x = 0.06mm$. Figure 7a plots the evolution of the modulus of the damage activation function ($|\phi_I|$), showing a convergence in 5-6 iterations. The Fig.7b plots the evolution of the damage variables of the three Gauss points showing the following: at the first iteration of the global NR method (FE NR iter. 1) three different values of the damage are obtained after convergence; at the last iterations (FE NR iter. 8) the same value of damage is correctly obtained for all the three Gauss points. Indeed, the correct solution for a uniform stress field is a uniform damage evolution along the embedded interface. The same results are obtained for all the nonlinear loading steps.

5 | FULL DEBONDING CONDITION

The bilinear response of the pure tensile test depicted in Fig.5b shows that the proposed formulation can also model the full debonding condition, with null traction at the interface and damage $\omega = 1$. But the full debonding condition ($\omega = 1$) cannot be analysed by the approach proposed in the previous section. In fact, the HEE formulation requires evaluation of the interface compliance matrix, defined in Eq.(46), which assumes an indeterminate form, even if only one point is fully debonded.

If the full debonding condition is reached in a number $1 \leq L_G \leq N_G$ of Gauss points ($\omega_J = 1$, with $J = 1, .., L_G$) of the side $\Gamma_1^{\bar{e}} = \partial\Omega_{\bar{e}} \cap \Gamma_0$ of the $\bar{e}$ element, the constitutive model imposes null tractions at these points ($\mathbf{s}_J = \mathbf{0}$, with $J = 1, .., L_G$). The full debonding condition states a linear problem which can be solved by a Lagrangian approach, for which the complementary energy function in Eq.(28) assumes the following form

$$\overline{\Pi}_c = \sum_{e=1}^{n_e}\left[\frac{1}{2}\mathbf{a}_e^T\left(\mathbf{C}_e + \mathbf{C}_e^{\Gamma}(\omega)\right)\mathbf{a}_e - \mathbf{a}_e^T\mathbf{H}_e\mathbf{u}_e + \mathbf{T}_e^T\mathbf{u}_e\right] - \mathbf{a}_{\bar{e}}^T\bar{\mathbf{H}}_{\bar{e}}\boldsymbol{\delta}_{\bar{e}}, \tag{64}$$

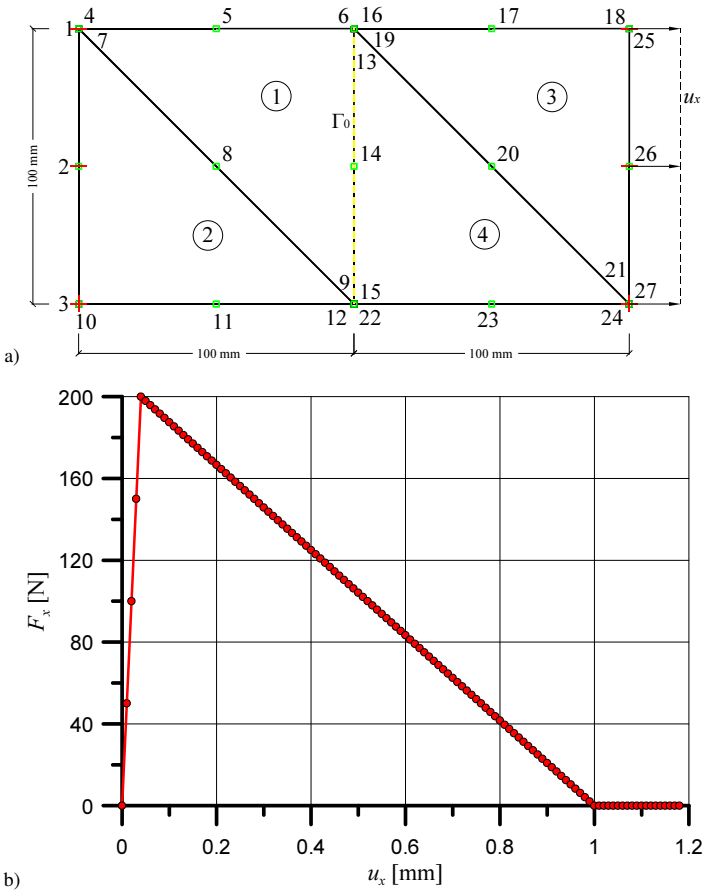

FIGURE 5 Pure tensile test with extrinsic interface embedded at the internal side of nodes 13-15: a) HEE discretization; b) response in terms of imposed displacement u_x and horizontal force F_x.

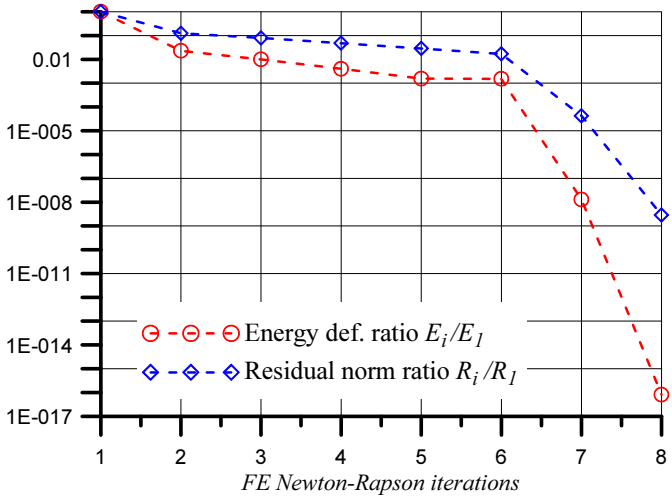

FIGURE 6 Convergence diagram of the iterative Newton-Rapson method, for the nonlinear loading step of imposed displacement $u_x = 0.06mm$, in terms of energy deformation ratio E_i/E_1 and residual norm ratio $> R_i/R_1$, between the current iteration and the first one.

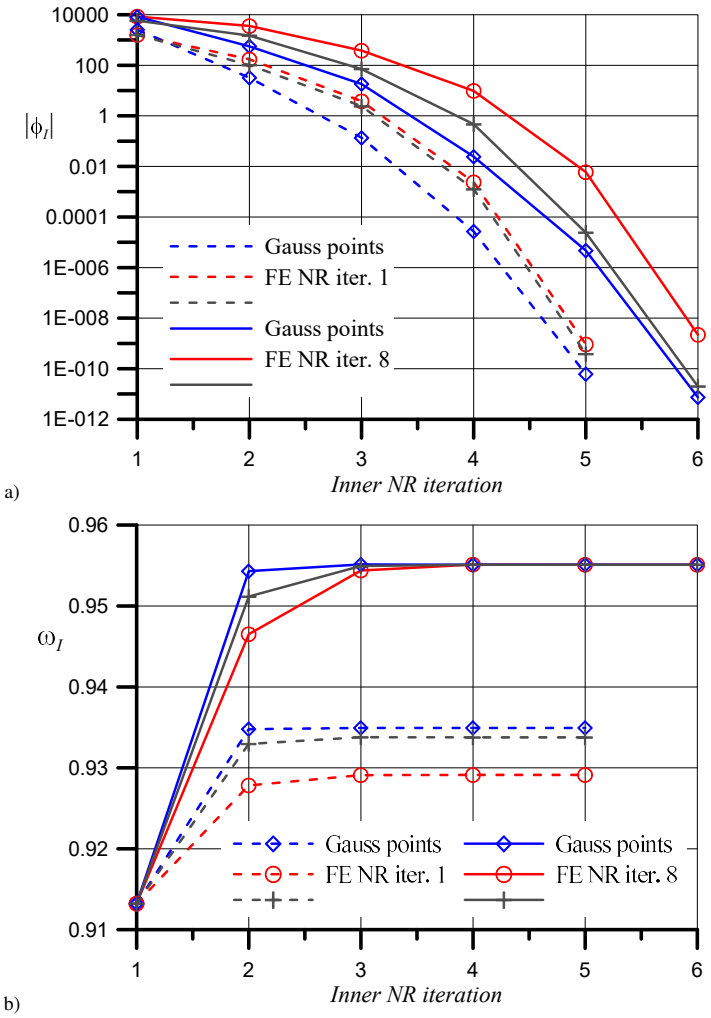

FIGURE 7 Convergence diagrams of the inner iterative Newton-Rapson method, for evaluation of the damage increments of the three Gauss points of the embedded interface, at the first iteration and at the last iteration of the loading step of imposed displacement $u_x = 0.06mm$: a) evolution of the modulus of the damage activation functions ($|\phi_I|$); b) evolution of the damage variables.

where $\bar{\mathbf{H}}_{\bar{e}} = \left[\mathbf{S}_1^T \mathbf{n}_1, \ldots, \mathbf{S}_{L_G}^T \mathbf{n}_{L_G}\right]$ and $\boldsymbol{\delta}_{\bar{e}} = \left[\boldsymbol{\delta}_1, \ldots, \boldsymbol{\delta}_{L_G}\right]^T$ is the vector of Lagrangian variables, which are the separation displacements between the two edges of the interface at the fully debonded Gauss points $\boldsymbol{\delta}_J = \left[\!\left[\boldsymbol{u}\left(\mathbf{x}_J\right)\right]\!\right]$, with $\mathbf{x}_J \in \Gamma_1^{\bar{e}}, J = 1, \ldots, L_G$.

The stationary conditions of the complementary energy function in Eq.(64) give the following equation for the element $\bar{e}$

$$\begin{bmatrix} \mathbf{C}_{\bar{e}} + \mathbf{C}_{\bar{e}}^{\Gamma}(\omega) & -\bar{\mathbf{H}}_{\bar{e}} & -\mathbf{H}_{\bar{e}} \\ -\bar{\mathbf{H}}_{\bar{e}}^T & \mathbf{0} & \mathbf{0} \\ -\mathbf{H}_{\bar{e}}^T & \mathbf{0} & \mathbf{0} \end{bmatrix} \begin{bmatrix} \mathbf{a}_{\bar{e}} \\ \boldsymbol{\delta}_{\bar{e}} \\ \mathbf{u}_{\bar{e}} \end{bmatrix} = \begin{bmatrix} \mathbf{0} \\ \mathbf{0} \\ -\mathbf{q}_{\bar{e}} \end{bmatrix}. \tag{65}$$

5.1 | Elastic loading step

For a loading step, without any damage increment, the vectors $\mathbf{a}_{\bar{e}}$ and $\boldsymbol{\delta}_{\bar{e}}$ can be condensed out of Eq.(65) and the solution for the HEE with fully debonded interface, can be written as

$$\boldsymbol{\delta}_{\bar{e}} = \left[\bar{\mathbf{H}}_{\bar{e}}^T \left(\mathbf{C}_{\bar{e}} + \mathbf{C}_{\bar{e}}^{\Gamma}\right)^{-1} \bar{\mathbf{H}}_{\bar{e}}\right]^{-1} \bar{\mathbf{H}}_{\bar{e}}^T \left(\mathbf{C}_{\bar{e}} + \mathbf{C}_{\bar{e}}^{\Gamma}\right)^{-1} \mathbf{H}_{\bar{e}}\, \mathbf{u}_{\bar{e}} \tag{66}$$

$$\mathbf{a}_{\bar{e}} = \left(\mathbf{C}_{\bar{e}} + \mathbf{C}_{\bar{e}}^{\Gamma}\right)^{-1} \left(\bar{\mathbf{H}}_{\bar{e}} \boldsymbol{\delta}_{\bar{e}} + \mathbf{H}_{\bar{e}} \mathbf{u}_{\bar{e}}\right) \tag{67}$$

$$\mathbf{q}_{\bar{e}} = \mathbf{H}_{\bar{e}}^T \mathbf{a}_{\bar{e}}. \tag{68}$$

Finally, the relevant elastic stiffness matrix is

$$\begin{aligned}\mathbf{K}_{\bar{e}} = \mathbf{H}_{\bar{e}}^T \left(\mathbf{C}_{\bar{e}} + \mathbf{C}_{\bar{e}}^{\Gamma}\right)^{-1} \bar{\mathbf{H}}_{\bar{e}} \left[\bar{\mathbf{H}}_{\bar{e}}^T \left(\mathbf{C}_{\bar{e}} + \mathbf{C}_{\bar{e}}^{\Gamma}\right)^{-1} \bar{\mathbf{H}}_{\bar{e}}\right]^{-1} \bar{\mathbf{H}}_{\bar{e}}^T \left(\mathbf{C}_{\bar{e}} + \mathbf{C}_{\bar{e}}^{\Gamma}\right)^{-1} \mathbf{H}_{\bar{e}} + \\ + \mathbf{H}_{\bar{e}}^T \left(\mathbf{C}_{\bar{e}} + \mathbf{C}_{\bar{e}}^{\Gamma}\right)^{-1} \mathbf{H}_{\bar{e}},\end{aligned} \tag{69}$$

which can be numerically evaluated by simple static condensation of the first two vectors of variables ($\mathbf{a}_{\bar{e}}$ and $\boldsymbol{\delta}_{\bar{e}}$) to the third one in Eq.(65).

The proposed approach gives the exact solution of an elastic loading step of an element with an embedded interface which is fully debonded at some or all of the Gauss integration points.

5.2 | Damaging loading step

The full debonding condition in a HEE can be combined with the violation of the damage activation function in other integration points, which require the evaluation of the relevant increment of the damage variables, for a known nodal displacement vector $\mathbf{u}_{\bar{e}}$. This mathematical problem has to be solved for the whole HEE with the embedded interface, and it requires the evaluation of the damage increment, the generalized stress and the separation displacement, which have to verify together the element Equation (65), the damage activation function and relevant flow rules in their discrete form in Eqs.(48-52). The index $\bar{e}$ is omitted hereafter.

The damage activation condition is violated in a number M_G of Gauss points ($\phi_J > 0$, with $J = 1, .., M_G$), with $1 \leq M_G \leq N_G$, and the full debonding condition is reached in a number L_G of Gauss points ($\omega_J = 1$, with $J = 1, .., L_G$), with $1 \leq L_G \leq N_G - M_G$. The two sets of nodes can belong to the same element side or to different sides. The constitutive consistency condition requires a vector of damage increment $\Delta\bar{\boldsymbol{\omega}}$, as defined in Eq.(53), generalized stress $\bar{\mathbf{a}}$ and separation displacement $\bar{\boldsymbol{\delta}}$, which has to verify the vector of violated consistency conditions in the whole interface element $\boldsymbol{\Phi}\left(\bar{\mathbf{a}}, \bar{\boldsymbol{\delta}}, \Delta\bar{\boldsymbol{\omega}}\right) = \mathbf{0}$, defined in Eq.(55). This solution also has to verify Eq.(65) of the HEE, for a known nodal displacement vector $\mathbf{u}$, which can be written in the following residual form

$$\begin{aligned}&\mathbf{R}\left(\bar{\mathbf{a}}, \bar{\boldsymbol{\delta}}, \Delta\bar{\boldsymbol{\omega}}\right) = \left[\mathbf{C} + \mathbf{C}^{\Gamma}\left(\Delta\bar{\boldsymbol{\omega}}\right)\right] \bar{\mathbf{a}} - \bar{\mathbf{H}}\bar{\boldsymbol{\delta}} + \mathbf{H}\mathbf{u} = \mathbf{0} \\ &\quad s.t.\ \bar{\mathbf{H}}^T \bar{\mathbf{a}} = \mathbf{0}.\end{aligned} \tag{70}$$

This mathematical problem can be solved by the iterative Newton-Rapson strategy proposed in Section (4.3), which is defined in the following matrix form

$$\begin{bmatrix} \mathbf{C} + \mathbf{C}^{\Gamma} & -\bar{\mathbf{H}} & \mathbf{K}_{\omega} \\ -\bar{\mathbf{H}}^T & \mathbf{0} & \mathbf{0} \\ \mathbf{K}_{\omega}^T & \mathbf{0} & \mathbf{K}_{\phi} \end{bmatrix} \begin{bmatrix} d\bar{\mathbf{a}} \\ d\bar{\boldsymbol{\delta}} \\ d\Delta\bar{\boldsymbol{\omega}} \end{bmatrix} = \begin{bmatrix} \mathbf{0} \\ \mathbf{0} \\ -\boldsymbol{\Phi}^i \end{bmatrix} \tag{71}$$

The iterative solution of Eq.(71) can be updated by $\Delta\bar{\boldsymbol{\omega}}^{i+1} = \Delta\bar{\boldsymbol{\omega}}^i + d\Delta\bar{\boldsymbol{\omega}}$, $\bar{\boldsymbol{\delta}}^{i+1} = \bar{\boldsymbol{\delta}}^i + d\bar{\boldsymbol{\delta}}$, whereas the updated separation displacements and the updated generalized stress are directly evaluated as

$$\begin{aligned}\boldsymbol{\delta}^{i+1} = &\left[\bar{\mathbf{H}}^T \left(\mathbf{C} + \mathbf{C}^{\Gamma}\left(\Delta\bar{\boldsymbol{\omega}}^{i+1}\right)\right)^{-1} \bar{\mathbf{H}}\right]^{-1} \cdot \\ &\cdot \bar{\mathbf{H}}^T \left(\mathbf{C} + \mathbf{C}^{\Gamma}\left(\Delta\bar{\boldsymbol{\omega}}^{i+1}\right)\right)^{-1} \mathbf{H}\,\mathbf{u}\end{aligned} \tag{72}$$

$$\bar{\mathbf{a}}^{i+1} = \left(\mathbf{C} + \mathbf{C}^{\Gamma}\left(\Delta\bar{\boldsymbol{\omega}}^{i+1}\right)\right)^{-1} \left(\bar{\mathbf{H}}\bar{\boldsymbol{\delta}}^{i+1} + \mathbf{H}\mathbf{u}\right), \tag{73}$$

with quadratic convergence of the proposed iterative formulation.

6 | NUMERICAL SIMULATION

The formulation developed was implemented in the finite element code FEAP[56] for a nine-node triangular HEE with quadratic stress fields and with extrinsic interface implicitly embedded at all element side, but the interface can activate only at one side per element. The implementation prevents the double opening of the same interface, that is the opening of the interface for two adjacent elements at the common side. A binary variable for each node of the mesh saves the information of the interface activation. When the activation condition is attained at an element side the binary variables of the three nodes are saved as active, so the activation condition of the adjacent element is not checked and the relevant embedded interface is not opened. This implementation is capable of analysing problem of delamination and crack propagation at any element side; indeed, if the interface opening condition is attained at a second side of an element, the same condition will be verified at the side of the adjacent element, where the crack will propagate. The numerical simulations of a pure mode I delamination test and two crack propagation tests were performed and the results are presented in the following Sections.

6.1 | DCB test

The delamination test is the pure mode I Double Cantilever Beam Test (DCBT) on an end-notched specimen with crack length $a = 50mm$, height of the two legs $h = 3mm$ and specimen width $b = 20mm$. The DCBT with the specimen sizes is represented in Fig.8. The bulk is modelled as isotropic and linear elastic with Young's modulus $E = 111\,900\,N/mm^2$ and Poisson's ratio $\nu = 0.2$ (standard homogenized parameters for carbon/epoxy composite material). The extrinsic interface constitutive parameters are defined by the fracture energies $G_I = G_{II} = 1N/mm$ and tensile strength $s_0 = 5\,N/mm^2$.

The analytical solutions of the DCBT is known in literature (see for instance[24]) and developed in the framework of bending Beam theory and linear elastic Fracture Mechanics (BFM) and it is given, in terms of imposed displacement u and load P by the following equations

$$\begin{aligned} u &= 4a^2\sqrt{\frac{G_I}{3\bar{E}h^3}} \\ P &= \frac{3\bar{E}I}{2a^3}u \end{aligned} \tag{74}$$

with $I = bh^3/12$ and $\bar{E} = E$ under plane stress conditions and $\bar{E} = E/(1-\nu^2)$ under plane strain conditions. The proposed

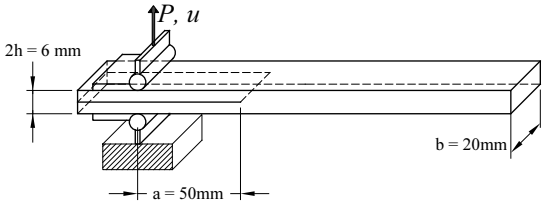

FIGURE 8 Sizes and geometry of specimen for the double cantilever beam test.

formulation of HEE with embedded interface can be used to model both the delamination surface and the pre-cracked one. The former surface is modelled as a sound embedded interface, with null initial damage, and the latter one is defined as a fully damaged embedded interface (with $\omega = 1$), and the positions of the two surfaces are assigned as input conditions. The pre-cracked surface and the delamination one are not discretized by specific interface elements and additional degrees of freedom, since for this approach they are actually not required. The results of the delamination test performed by the HEE with embedded extrinsic interface are compared to the analytical solution and to the results obtained by the formulation proposed in Ref. [16], where the intrinsic interface is kinematically modelled by the eXtended finite element (XFEM) formulation. The intrinsic interface is modelled with an initial elastic behaviour with elastic stiffness $K_n = K_t = 50000N/mm^3$. The results are compared in Fig. 9 in terms of imposed vertical displacement u vs reaction force P, showing perfect matching between the two numerical solutions (HEE and XFEM). Moreover, the two numerical solutions reproduce the analytical one with good accuracy both in the descending damaging branch and in the elastic unloading one.

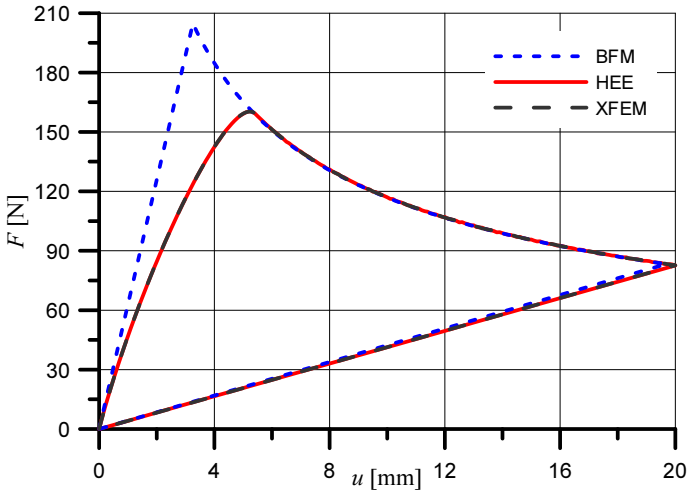

FIGURE 9 Response of double cantilever beam test, in terms of applied load vs imposed displacement of the analytical solution (BFM) and two numerical solutions based on HEE with embedded extrinsic interface and XFEM with intrinsic interface.

Motivations of the different responses in the initial elastic branch between the numerical solutions and the analytical one are well known in literature (see[16,57]) and are due to the two different delamination conditions, based on the linear elastic fracture mechanics theory for the analytical solution, with an ideally brittle traction-separation law, whereas in the CZMs the delamination condition produces a bilinear response with a smooth transition from the elastic behaviour to the fully debonded one. The maps of stress σ_x, σ_y and σ_{xy}, obtained by the HEE with embedded interface at four different loading conditions of imposed displacement $u = 5, 10, 15, 20$mm, are plotted in the deformed configuration in Figures 10, 11 and 12.

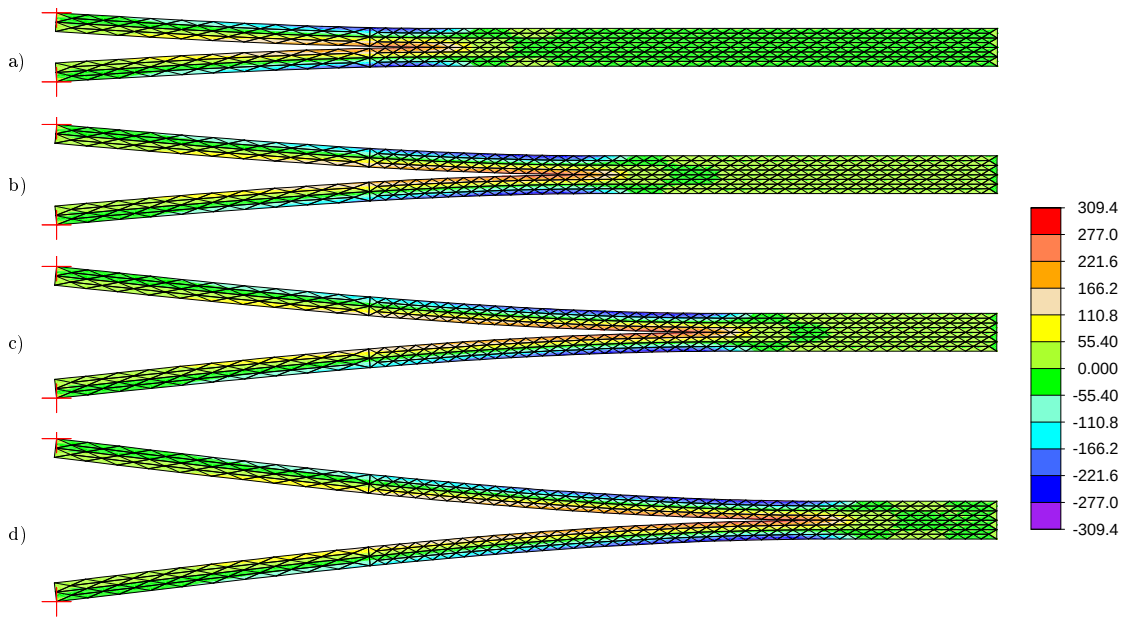

FIGURE 10 Map of normal stress σ_x [MPa] at the four different loading conditions: $u = 5, 10, 15, 20$mm.

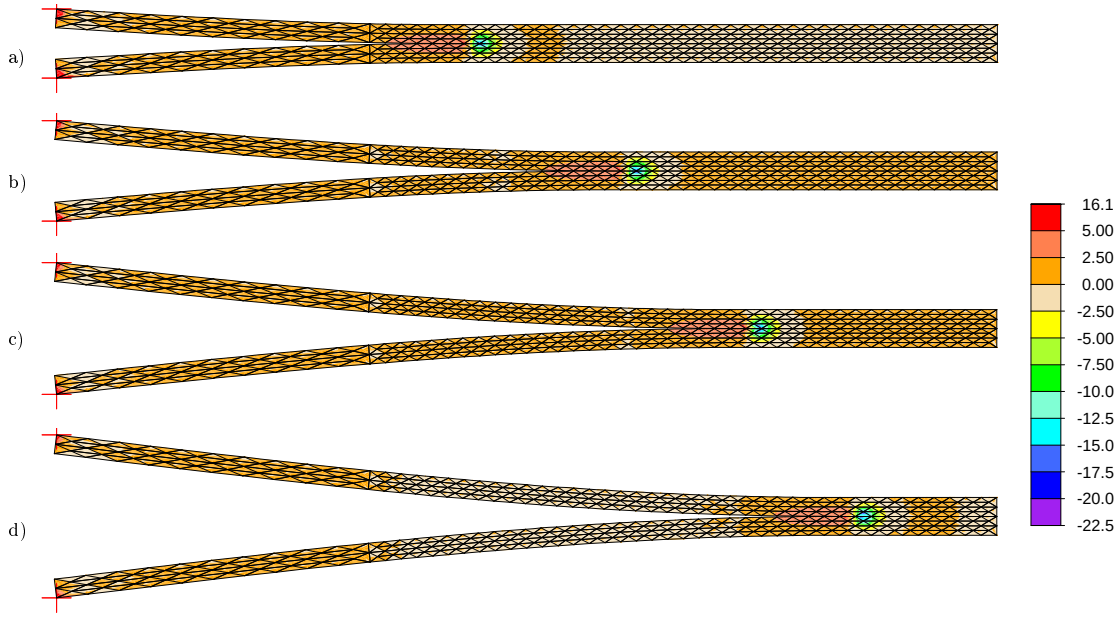

FIGURE 11 Map of normal stress σ_y [MPa] at the four different loading conditions: $u = 5, 10, 15, 20$mm.

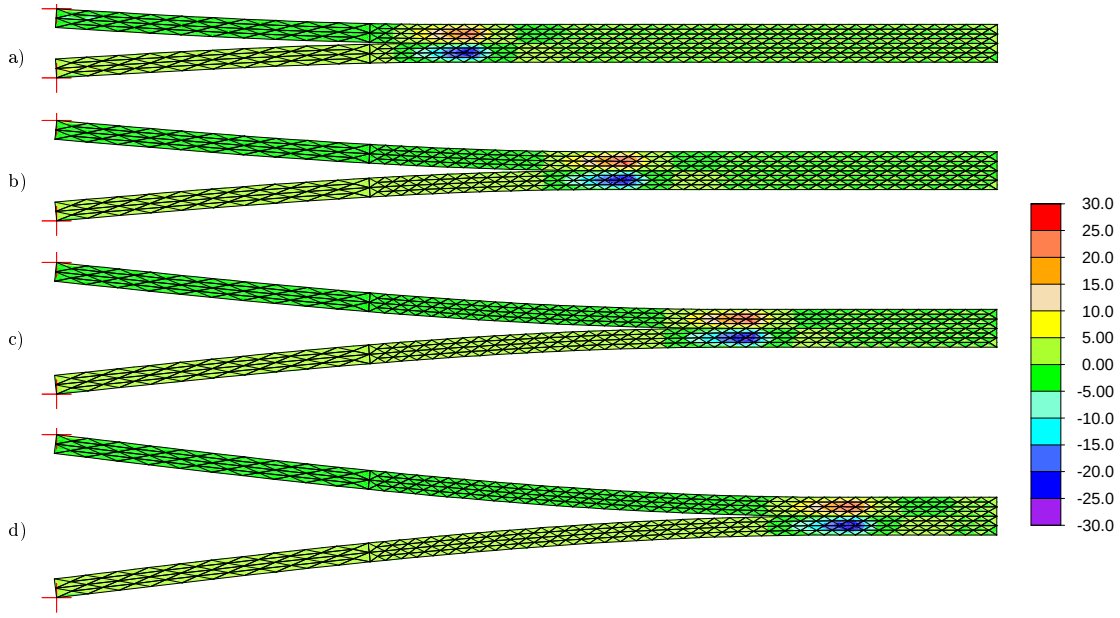

FIGURE 12 Map of tangential stress σ_{xy} [MPa] at the four different loading conditions: $u = 5, 10, 15, 20$mm.

6.2 | Double-cantilever-beam test with diagonal loads

The second numerical analysis is the quasi-static simulation of the mixed-mode crack propagation problem of the double-cantilever-beam (DCB) test with diagonal forces. The crack path is not fixed and the crack can develop in any element side where the tractions components attain the damage activation condition defined in the Section 4.1.

The experimental test is reported in Ref.[58] and is also analysed in Ref.[59] by smeared crack analysis, and in Refs.[60,17] by strong discontinuity approaches. Geometry and load setting of the experimental test are represented in Fig. 13a, with the plate

thickness 50.8 mm. The diagonal forces F1 increase until reaching 3.78 kN and then are kept constant. In the numerical simulation presented, the wedge forces F2 are modelled as reaction forces of imposed separation displacement, which increases monotonically. Part of the specimen is discretized with standard Displacement Based finite Elements (DBE) and the zone where the crack is expected to propagate is discretized with the proposed HEE formulation . The different discretized areas are shown in Fig.13a. The numerical simulation was performed with the two meshes represented in Figs.13b, c. In HEE the concentrated force F2 at the upper-right corner generates high stress level and, in order to avoid anomalous crack opening, the elements close to the corner are assumed as elastic.

The constitutive parameters of the bulk material and extrinsic interface are the following: $E = 30500 N/mm^2$, $\nu = 0.2$, $s_0 = 2 N/mm^2$, $G_I = 0.1 N/mm$. The results of the numerical simulations obtained with the two meshes are plotted in the Fig.14 in terms of applied load $F2$ and crack mouth opening displacement (CMOD). The results are compared with the experimental data reported in Ref.[58] and with the numerical results obtained by the embedded discontinuity finite element formulation and by the XFEM formulation in Ref.[17].

The load-CMOD curves obtained with the two meshes do not show significant differences from each other, and the results fit the other numerical data (DG and XFEM) and the experimental curve with good approximation.

The results of the numerical simulations are also presented by the maps of the maximum principal stress at the peak loading condition in the deformed configuration, showing the crack path, in Figures 15 a, b for mesh 1 and mesh 2. The further propagation of the crack obtained with the two meshes is represented in the Figures 16a, d in the deformed configuration, together with the maps of the maximum principal stress, at the following loading steps of CMOD values $\Delta u = 0.2mm$ and $\Delta u = 0.4mm$.

The crack paths obtained by the numerical simulations with the two meshes are also depicted in Fig.13a and compared with the experimental crack path, showing a good prediction, even though in the proposed formulation the crack is constrained to propagate only at the element sides.

A possible improvement of the proposed model, in order to overcome the mesh dependency of the numerical response, could be simple correction of the mesh geometry ahead of the crack tip, so that an element side is oriented along the maximum principal stress direction.

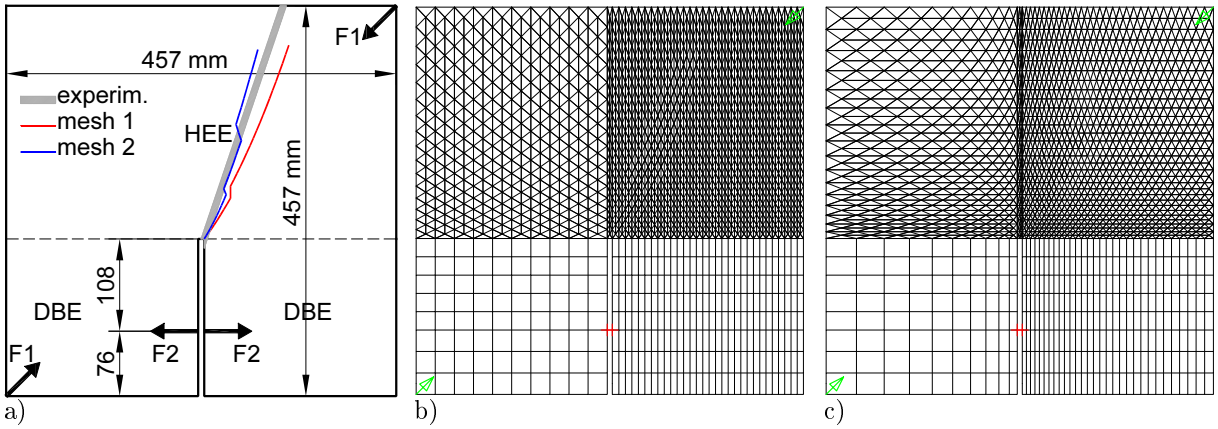

FIGURE 13 Double-cantilever-beam test with diagonal loads: a) sizes, geometry, loading condition and discretization zones; the experimental crack path and crack paths obtained with the two meshes ; b) mesh 1; c) mesh 2.

6.3 | Single-edge notched beam

The third numerical analysis is the quasi-static simulation of the mixed-mode crack propagation problem of the single-edge notched concrete beam. The results of the experimental tests are given in Ref.[61] where the crack path is also numerically predicted in the framework of linear elastic fracture mechanics. The crack propagation of this problem is also numerically reproduced in Ref.[44], by a discontinuous Galerkin finite element formulation with rigid-cohesive interface model at all the inter-element sides, and by the XFEM formulation in Ref.[62]. The model is analysed under plane stress conditions and the load level is governed by the arclength control of the crack mouth opening displacement (CMOD).

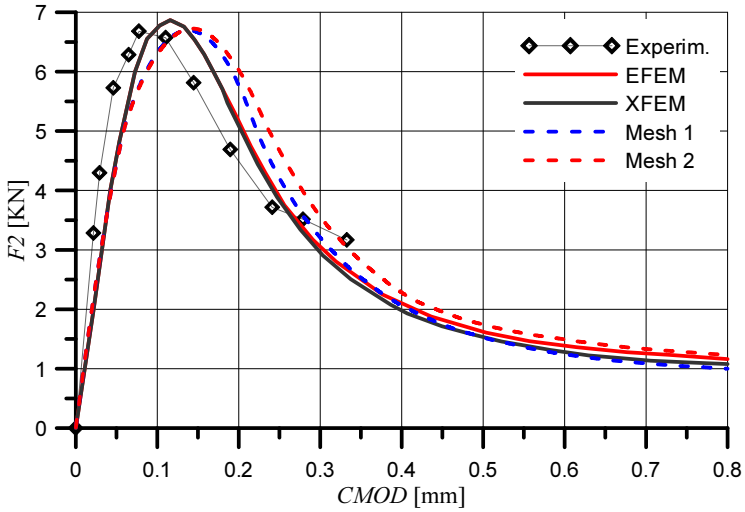

FIGURE 14 Responses of the numerical simulations of the double-cantilever-beam test with diagonal loads in terms of load $F2$ and crack mouth opening displacement (CMOD).

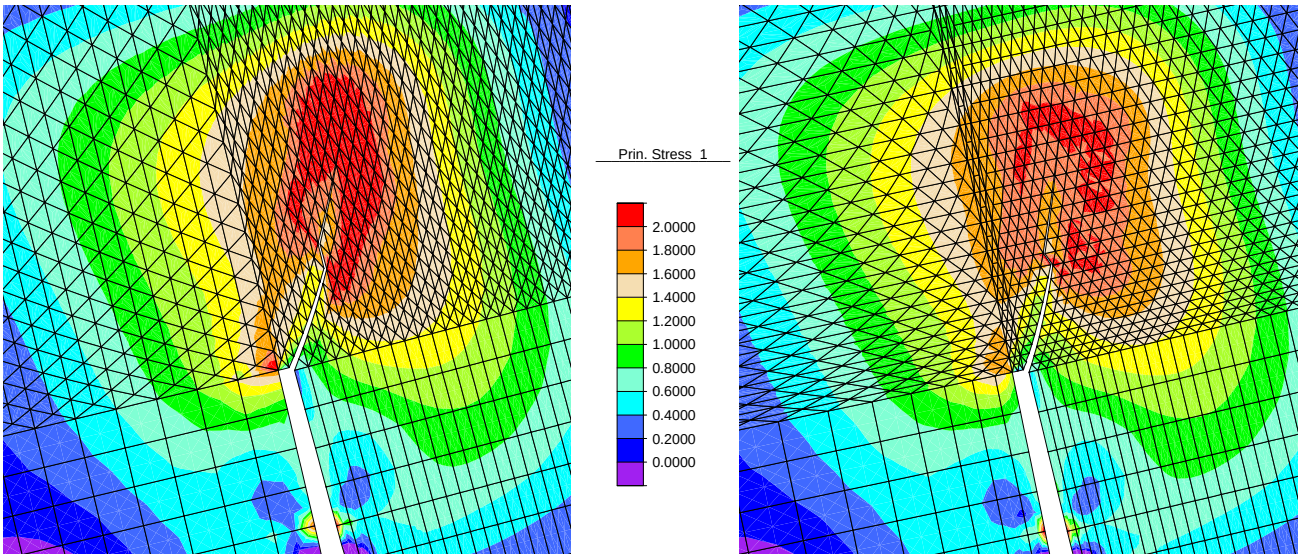

a) Mesh 1 b) Mesh 2

FIGURE 15 Maps of maximum principal stress σ_1 [MPa] at the crack tip, in the deformed configuration with the evolution of the crack, at the peak loading condition for: a) mesh 1; b) mesh 2.

The size and geometry of the specimen (thickness $t = 50mm$) with boundary and loading conditions are reported in Fig.17, where the experimental envelope of the crack is also plotted. The left hand side of the specimen is irrelevant from the mechanical point of view, being subjected to neither loads nor boundaries, and it is neglected in the domain discretization. Moreover, part of the specimen is discretized with standard displacement-based finite elements and only the zone where the crack is expected to propagate is discretized with the proposed HEE formulation. The different discretized areas are shown in Fig.17: the NO MESH area has not been discretized, the DBE area has been discretized with nine-node quadrilateral Displacement Based Element and the HEE area has been discretized with nine-node triangular hybrid equilibrium element, with extrinsic interface implicitly embedded at all the element sides. Due to the mesh dependency of the possible cracking paths, the numerical simulation was

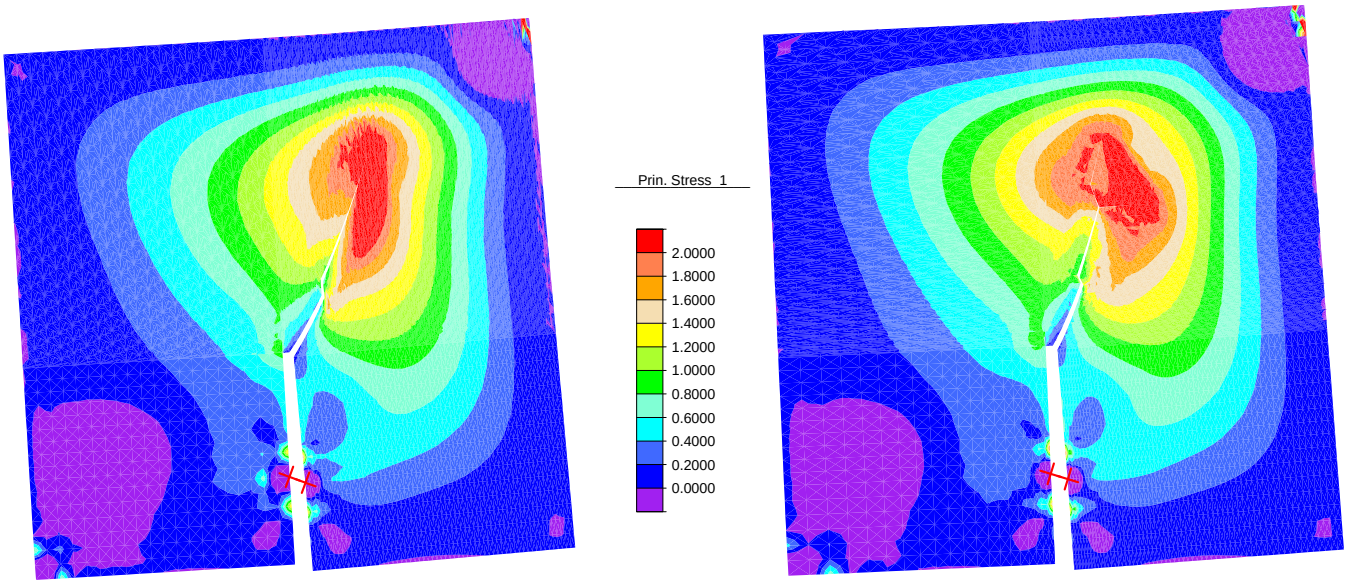

a) Mesh 1, $\Delta u = 0.2$mm b) Mesh 2, $\Delta u = 0.2$mm

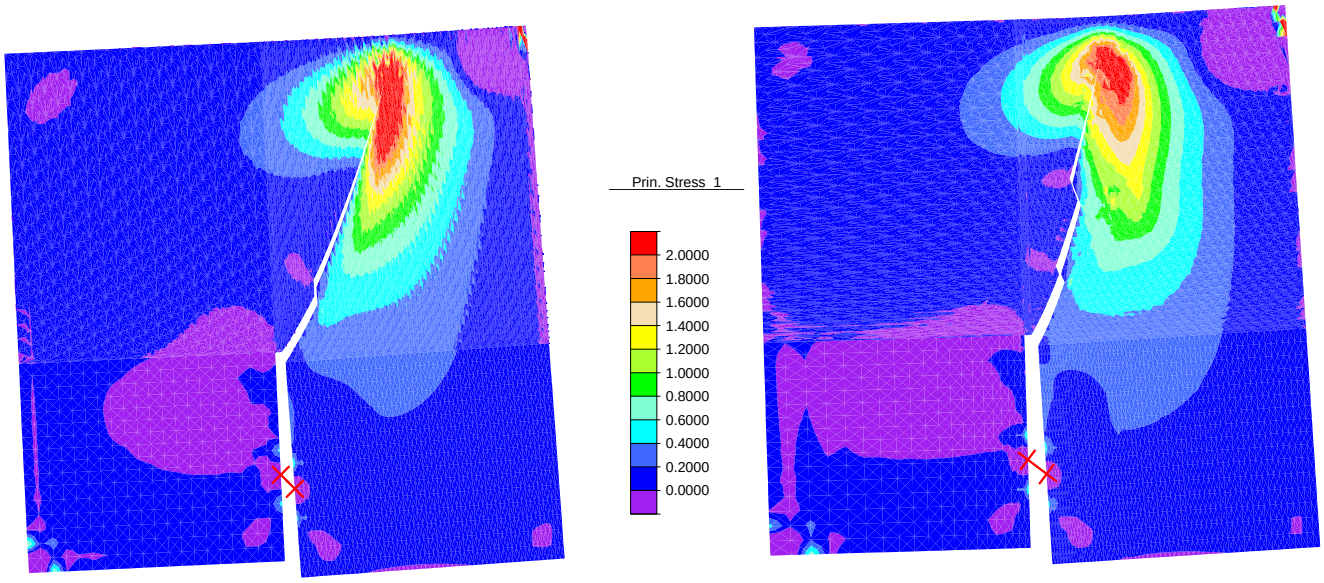

FIGURE 16 Maps of maximum principal stress σ_1 [MPa], in the deformed configuration with the evolution of the crack, for: a) mesh 1 for CMOD=$\Delta u = 0.2$; b) mesh 2 for CMOD=$\Delta u = 0.2$; c) mesh 1 for CMOD=$\Delta u = 0.4$; d) mesh 2 for CMOD=$\Delta u = 0.4$.

performed with the four different meshes plotted in the Figs.18 A, D. The four meshes present one finite element with two free boundary sides (external corner) at the right side of the crack and the relevant spurious kinematic modes have been restrained by the approach proposed in Ref.[52], by a rigid constrain between the vertical (or horizontal) degrees of freedom of the two corner nodes.

The constitutive parameters of the bulk material and extrinsic interface are: $E = 38000N/mm^2$, $\nu = 0.18$, $s_0 = 3N/mm^2$, $G_I = 0.069N/mm$. The results of the numerical simulations obtained with the four meshes are plotted in Fig.19 in terms of the applied load F and the CMOD. The results are compared with the numerical results obtained by a Discontinuous Galerkin (DG) finite element formulation in Ref.[44], with the numerical results obtained by the XFEM formulation in Ref.[62] and with the experimental envelope reported in Ref.[61]. The load-CMOD curves obtained with the four meshes do not show significant

differences one from each other, and the results fit the other numerical data (DG and XFEM) and the experimental envelope with good approximation.

The results of the numerical simulations are also represented by the maps of the maximum principal stress at three loading steps: the peak loading condition and the loading conditions obtained for the CMOD values $\Delta u = 0.2mm$ and $\Delta u = 0.4mm$. The maps of the maximum principal stress are plotted in the deformed configuration, showing the cracking path, in Figure 20 for mesh A and mesh B, and in Figure 21 for mesh C and mesh D. Figures 20 and 21 show similar maps of stress and similar cracking paths for the four different meshes.

Finally, the cracking path obtained by the proposed formulation with the four meshes are compared to the experimental crack envelope of crack trajectories in Fig. 22. Although the four meshes are not extremely fine, the high order stress fields defined in the proposed formulation, codiffusive at each element side and satisfying the homogeneous equilibrium equations, make it possible to capture the cracking paths and the overall response with good approximation for all the considered meshes.

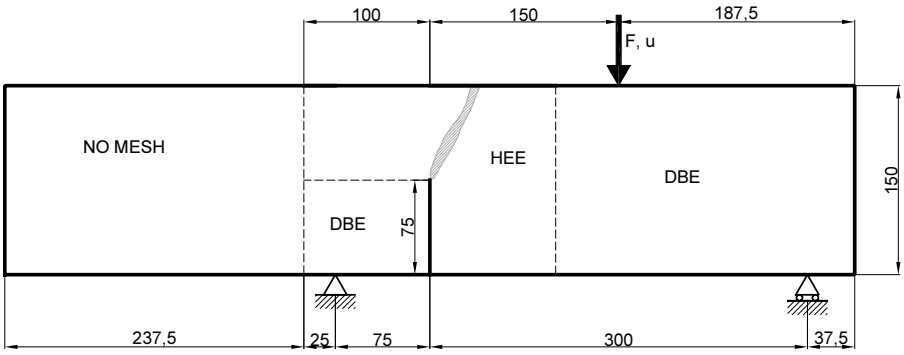

FIGURE 17 Sizes and geometry of specimen of the single-edge notched beam with the different discretization zones. The experimental envelope of crack trajectories is plotted in the hatched area.

7 | CLOSING REMARKS

The paper presents an innovative approach for the modelling of delamination and crack propagation at the inter-element interface of Hybrid Equilibrium Elements. The proposed formulation gives a solution which satisfies the homogeneous equilibrium equation in the whole domain and it allows one to introduces an extrinsic interface at every element side without any additional degree of freedom.

The paper also presents an interface extrinsic cohesive model, developed in the rigorous thermodynamic framework of damage mechanics. The proposed model produces a bilinear response with initially rigid behaviour. The damage activation condition of the extrinsic interface model is based on the tractions and its application is perfectly suitable for use with the high-order stress field of HEE.

The proposed formulation was implemented in a finite element code and the numerical simulations of one delamination problem and two crack propagation problems were carried out with different meshes. Although the meshes are not extremely fine, the high-order stress fields defined in the proposed formulation make it possible to capture the cracking paths and the overall response with good approximation for all the considered meshes.

The drawbacks of the proposed formulation are the following: firstly, the presence of spurious kinematic modes, but they are well known and can be controlled or restrained by means of some different approaches; secondly, the damage consistency condition and evaluation of the damage increments have to be performed for the whole HEE with embedded interface, rather than for the single integration point. This problem requires the resolution of an inner Newton-Rapson nonlinear problem for every HEE with damaging interface. However, the additional inner Newton-Raphson procedure has to be performed only for the few elements in the process zone, whereas pristine elements and full debonded elements behave elastically and without

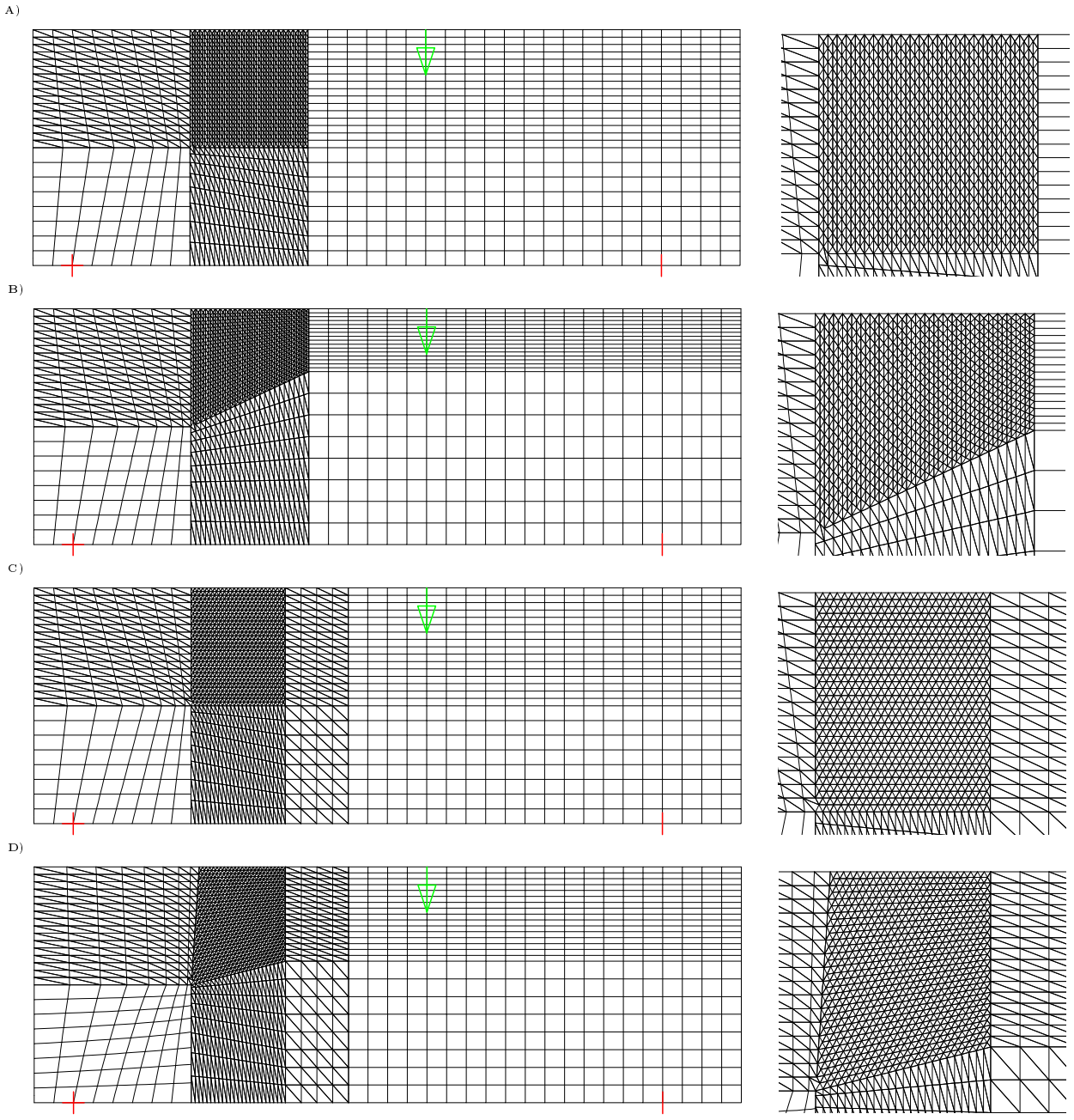

FIGURE 18 Meshes for the crack propagation analysis of the single-edge notched beam with the zoomed view at the part with the finest mesh.

any additional degree of freedom. On the contrary, the mixed formulation obliges the use of additional degrees of freedom (Lagrangian variables) in order to keep connected the independent nodes of all the couples of adjacent elements, for any loading step, either elastic or with cracking evolution. In DG approach all finite elements are discretized with independent nodes and the displacement continuity between independent nodes of adjacent elements is weakly enforced, but without additional degrees of freedom.

Future developments of the proposed model could be correction of the mesh geometry ahead the crack tip so that an element side is oriented along the maximum principal stress direction, in order to overcome the mesh dependency of the numerical response in crack propagation problems; the formulation of the HEE for the dynamic analysis of fragmentation problems and

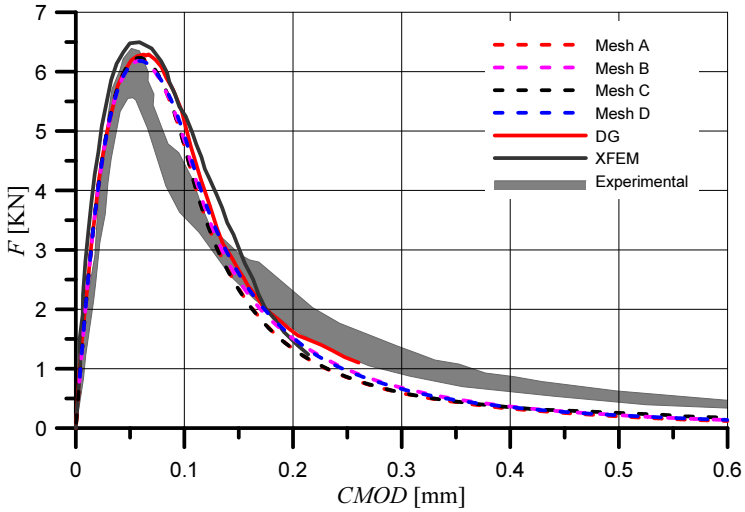

FIGURE 19 Responses of the numerical simulations of the single-edge notched beam in terms of load F and crack mouth opening displacement (CMOD).

for correct evaluation of wave speed. Finally, the comparison of computational time between the proposed model and existing models (mixed model and DG) could be performed.

ACKNOWLEDGMENT

The financial support of the Italian Ministry for University and Research (MIUR), under the Grant PRIN-2015, Project No. 2015LYYXA8, "Multiscale mechanical models for the design and optimization of microstructured smart materials and metamaterials" is gratefully acknowledged.

Financial disclosure

None reported.

Conflict of interest

The authors declare no potential conflict of interests.

How to cite this article: Parrinello F., (2020), Hybrid equilibrium element with inter-element interface for the analysis of delamination and crack propagation problems, *Int.Jou.Num.Meth.Eng.*, *2020;00:1–6*.

APPENDIX

A CONSISTENT ELEMENT STIFFNESS MATRIX

The proposed constitutive law produces a non linear numerical response and it can be effectively implemented in a finite element code, with quadratic convergence, if the element consistent tangent operator, the derivative of the nodal force vector with respect to the nodal displacement vector, is correctly defined.

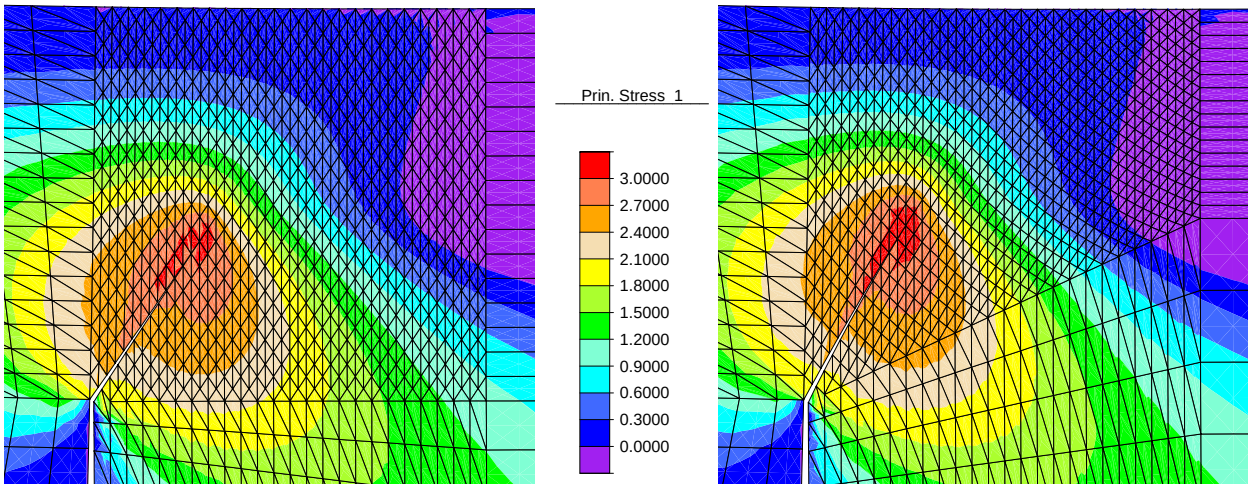

Mesh A, peak loading condition

Mesh B, peak loading condition

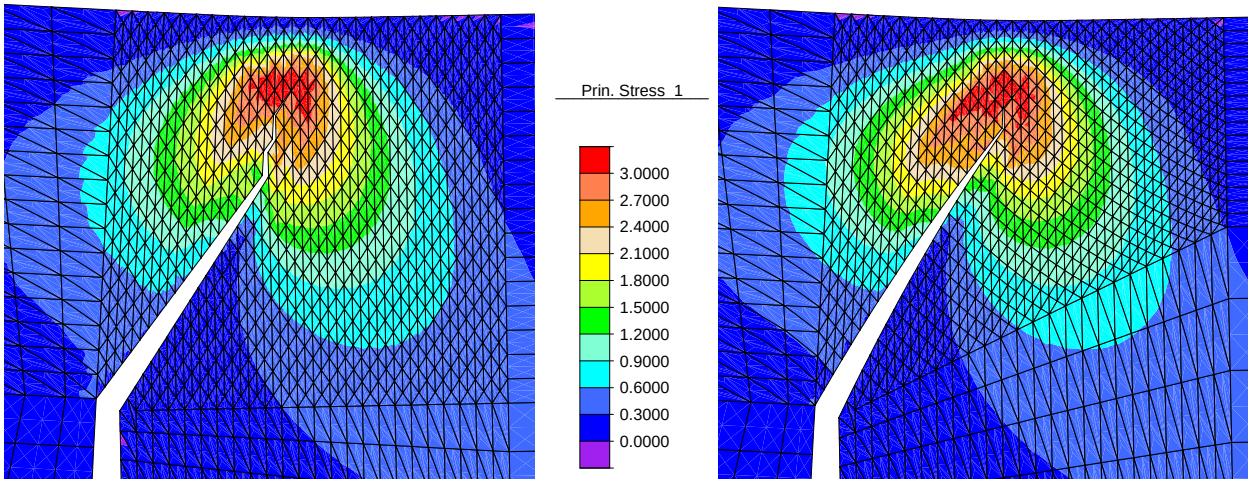

Mesh A, $\Delta u = 0.2$mm

Mesh B, $\Delta u = 0.2$mm

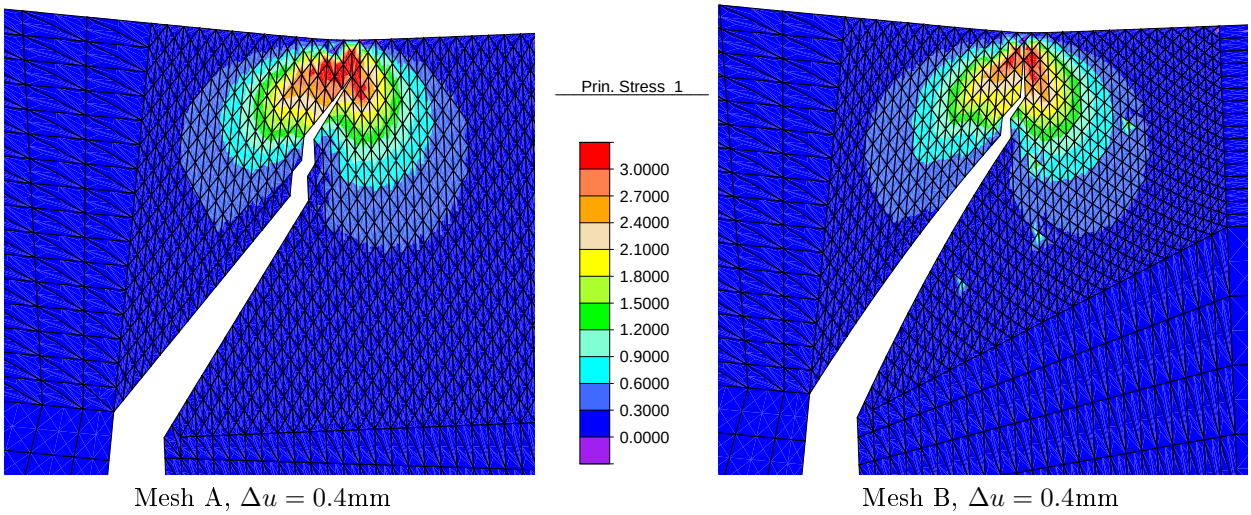

Mesh A, $\Delta u = 0.4$mm

Mesh B, $\Delta u = 0.4$mm

FIGURE 20 Maps of maximum principal stress σ_1 [MPa] for mesh A and mesh B, in the deformed configuration with the evolution of the crack, at the three different loading conditions: the peak loading condition and the loading conditions obtained for the values of CMOD $\Delta u = 0.2$, $\Delta u = 0.4$.

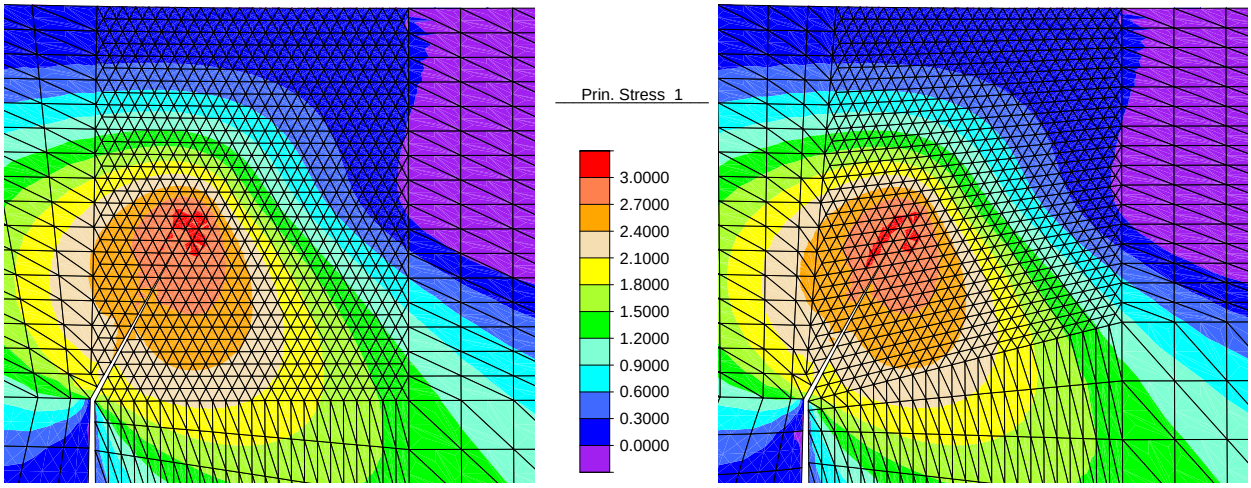

Mesh C, peak loading condition

Mesh D, peak loading condition

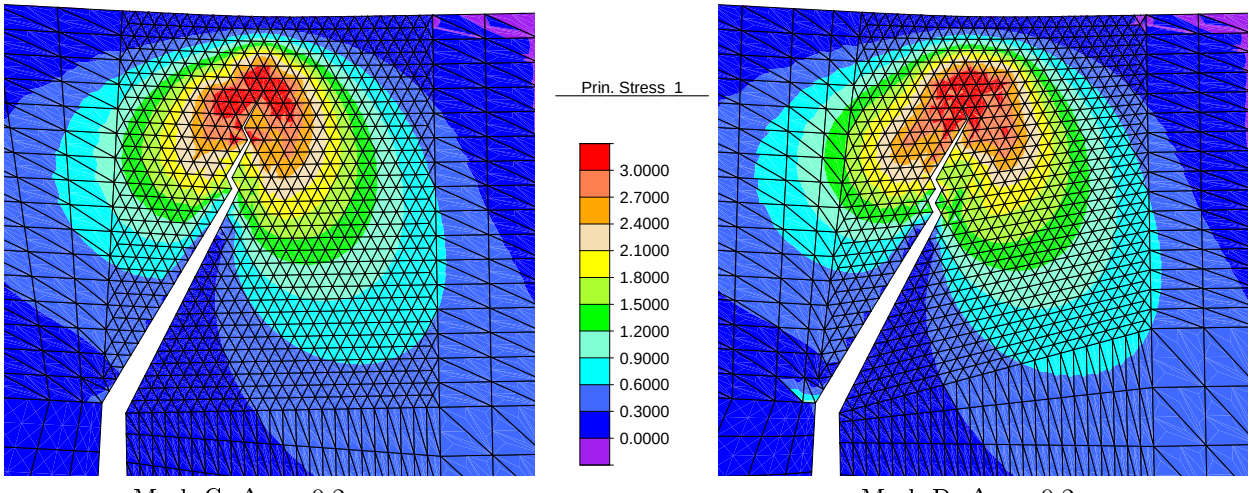

Mesh C, $\Delta u = 0.2$mm

Mesh D, $\Delta u = 0.2$mm

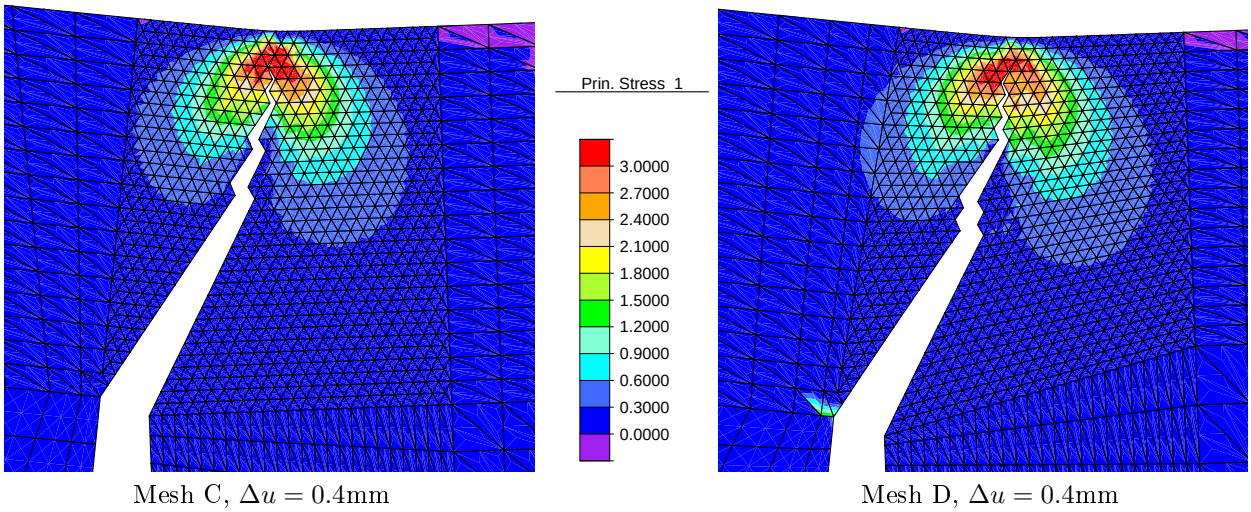

Mesh C, $\Delta u = 0.4$mm

Mesh D, $\Delta u = 0.4$mm

FIGURE 21 Maps of maximum principal stress σ_1 [MPa] for meshes C and D, in the deformed configuration with the evolution of the crack, at the three different loading conditions: the peak loading condition and the loading conditions obtained for the values of CMOD $\Delta u = 0.2$, $\Delta u = 0.4$.

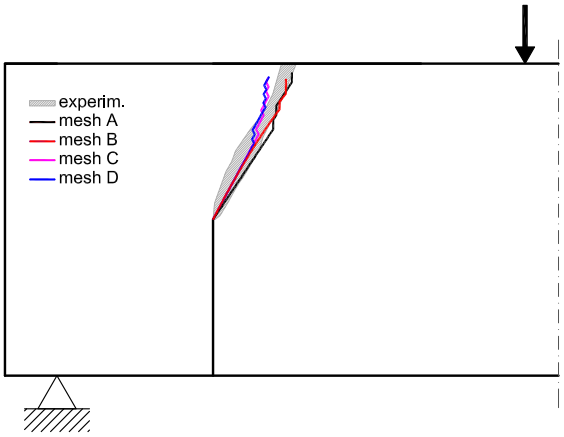

FIGURE 22 Crack paths obtained by the numerical simulation with the four meshes compared with the experimental crack path envelope.

The nodal force vector $\mathbf{q}$ of a HEE with not fully debonded integration points is defined in Eq.(30) and for an elastic loading step ($\phi(x) < 0$ in $\Gamma^e \cap \Gamma_0$) the consistent tangent stiffness matrix coincides with the elastic stiffness matrix, that is

$$\mathbf{K}^{cs} = \frac{d\mathbf{q}}{d\mathbf{u}} = \mathbf{K}^{el} = \mathbf{H}_e^T \left(\mathbf{C}_e + \mathbf{C}_e^{\Gamma}(\boldsymbol{\omega})\right)^{-1} \mathbf{H}_e. \tag{A1}$$

For an elastic loading step, the consistent stiffness matrix of a HEE with some fully debonded Gauss points coincides with the elastic one defined in Eq.(69).

For a nonlinear loading step, let an HEE be considered with the damage activation condition attained in M_G integration points, for which the damage activation function is null at the end of the iterative process described in Section 4.3, that is $\phi_I = 0$ for $I = 1, \dots, M_G$, or in compact form $\boldsymbol{\Phi} = \mathbf{0}$. The considered HEE is not subjected to any full debonding condition ($\omega < 1$ in $\Gamma^e \cap \Gamma_0$) and the residual in Eq.(54) and the nodal force vector can be rewritten in the following incremental form

$$\begin{aligned} d\mathbf{R} &= \frac{\partial \mathbf{R}}{\partial \mathbf{a}} d\mathbf{a} + \frac{\partial \mathbf{R}}{\partial \Delta\bar{\boldsymbol{\omega}}} d\Delta\bar{\boldsymbol{\omega}} + \frac{\partial \mathbf{R}}{\partial \mathbf{u}} d\mathbf{u} = \\ &= \left[\mathbf{C} + \mathbf{C}^{\Gamma}(\Delta\bar{\boldsymbol{\omega}})\right] d\mathbf{a} + \mathbf{K}_{\omega} d\Delta\bar{\boldsymbol{\omega}} - \mathbf{H} d\mathbf{u} = 0 \end{aligned} \tag{A2}$$

$$d\mathbf{q} = \mathbf{H}^T d\mathbf{a}. \tag{A3}$$

Moreover, under an increasing loading condition, the loading-unloading constitutive condition of Eq.(52) can be written for the M_G damage active points as

$$d\boldsymbol{\Phi} = \frac{\partial \boldsymbol{\Phi}}{\partial \mathbf{a}} d\mathbf{a} + \frac{\partial \boldsymbol{\Phi}}{\partial \Delta\bar{\boldsymbol{\omega}}} d\Delta\bar{\boldsymbol{\omega}} = \mathbf{K}_{\omega}^T d\mathbf{a} + \mathbf{K}_{\phi} d\Delta\bar{\boldsymbol{\omega}} = 0 \tag{A4}$$

where the vector $\boldsymbol{\Phi}$ only collects the damage activation function of the damage active points.

Equations (A2), (A3) and (A4) can be collected in the following matrix notation

$$\begin{bmatrix} d\mathbf{R} \\ d\boldsymbol{\Phi} \\ -d\mathbf{q} \end{bmatrix} = \begin{bmatrix} \mathbf{C} + \mathbf{C}^{\Gamma}(\Delta\bar{\boldsymbol{\omega}}) & \mathbf{K}_{\omega} & -\mathbf{H} \\ \mathbf{K}_{\omega}^T & \mathbf{K}_{\phi} & \mathbf{0} \\ -\mathbf{H}^T & \mathbf{0} & \mathbf{0} \end{bmatrix} \begin{bmatrix} d\mathbf{a} \\ d\Delta\bar{\boldsymbol{\omega}} \\ d\mathbf{u} \end{bmatrix} = \begin{bmatrix} \mathbf{0} \\ \mathbf{0} \\ -d\mathbf{q} \end{bmatrix} \tag{A5}$$

and the consistent stiffness matrix, for an HEE with active damage points and without fully debonded points, can be numerically obtained by static condensation of the first two blocks of variables, that are $d\mathbf{a}$ and $d\Delta\bar{\boldsymbol{\omega}}$, to the third block. The consistent stiffness matrix is symmetric and defined as

$$\mathbf{K}^{cs} = \mathbf{H}^T \left[\mathbf{C} + \mathbf{C}^{\Gamma}(\Delta\bar{\boldsymbol{\omega}}) - \mathbf{K}_{\omega} \mathbf{K}_{\phi}^{-1} \mathbf{K}_{\omega}^T\right]^{-1} \mathbf{H}. \tag{A6}$$

The HEE with fully debonded points and without any damage increment behaves elastically and the relevant stiffness matrix is defined in Eq.(69). The equation of an HEE with fully debonded points and active damage points is written in residual form in Eq.(70), and together with the constitutive consistency condition at the M_G active Gauss points, that is $\boldsymbol{\Phi} = \mathbf{0}$, and under the

relevant loading-unloading constitutive condition $d\boldsymbol{\Phi} = \mathbf{0}$ defined in Eq.(A4), these equations can be written in the following incremental form

$$\begin{bmatrix} d\mathbf{R} \\ d\mathbf{R}_\delta \\ d\boldsymbol{\Phi} \\ -d\mathbf{q} \end{bmatrix} = \begin{bmatrix} \mathbf{C} + \mathbf{C}^\Gamma(\Delta\bar{\boldsymbol{\omega}}) & -\bar{\mathbf{H}} & \mathbf{K}_\omega & -\mathbf{H} \\ -\bar{\mathbf{H}}^T & \mathbf{0} & \mathbf{0} & \mathbf{0} \\ \mathbf{K}_\omega^T & \mathbf{0} & \mathbf{K}_\phi & \mathbf{0} \\ -\mathbf{H}^T & \mathbf{0} & \mathbf{0} & \mathbf{0} \end{bmatrix} \begin{bmatrix} d\mathbf{a} \\ d\boldsymbol{\delta} \\ d\Delta\bar{\boldsymbol{\omega}} \\ d\mathbf{u} \end{bmatrix} = \begin{bmatrix} \mathbf{0} \\ \mathbf{0} \\ \mathbf{0} \\ -d\mathbf{q} \end{bmatrix}. \tag{A7}$$

Due to the symmetry of the coefficients matrix, the consistent stiffness matrix is symmetric and can be numerically obtained by static condensation of the first three blocks of variables to the last one.

The Equations (A5) and (A7) suggest that a single NR iterative approach could be adopted and generalized stress $\mathbf{a}$ and displacement $\mathbf{u}$ computed at each iteration after updating all damage variable (explicitly for the proposed constitutive law). Nevertheless, the proposed approach is based on the stationary condition of the complementary energy functional, which is defined in the space of statically admissible solutions, and the use of the inner NR provides solutions that verify the domain equilibrium equation for all the elements.

References

1. Polizzotto C. Unified thermodynamic framework for nonlocal/gradient continuum theories. *European Journal of Mechanics, A/Solids* 2003; 22(5): 651-668.

2. Benvenuti E, Borino G, Tralli A. A thermodynamically consistent nonlocal formulation for damaging materials. *European Journal of Mechanics, A/Solids* 2002; 21(4): 535-553. doi: 10.1016/S0997-7538(02)01220-2

3. Borino G, Failla B, Parrinello F. A symmetric nonlocal damage theory. *International Journal of Solids and Structures* 2003; 40(13-14): 3621-3645.

4. Verhoosel CV, Borst dR. A phase-field model for cohesive fracture. *International Journal for Numerical Methods in Engineering* 2013; 96(1): 43-62.

5. Paggi M, Corrado M, Reinoso J. Fracture of solar-grade anisotropic polycrystalline Silicon: A combined phase field–cohesive zone model approach. *Computer Methods in Applied Mechanics and Engineering* 2018; 330: 123 - 148.

6. Giambanco G, La Malfa Ribolla E. A phase-field model for strain localization analysis in softening elastoplastic materials. *International Journal of Solids and Structures* 2019; 172-173: 84-96. doi: 10.1016/j.ijsolstr.2019.04.001

7. Simo J, Oliver J, Armero F. An Analysis of Strong Discontinuities induced by strain softening in rate-independent inelastic solids. *Computational Mechanics* 1993; 12: 277-296. doi: 10.1007/BF00372173

8. Jirasek M. Comparative study on finite elements with embedded discontinuities. *Computer Methods in Applied Mechanics and Engineering* 2000; 188: 307-330.

9. Oliver J, Huespe A. Theoretical and computational issues in modelling material failure in strong discontinuity scenarios. *Computer Methods in Applied Mechanics and Engineering* 2004; 193(27): 2987 - 3014. Computational Failure Mechanics for Geomaterialsdoi: https://doi.org/10.1016/j.cma.2003.08.007

10. Huespe AE, Oliver J. *Crack Models with Embedded Discontinuities*: 99–159; Vienna: Springer Vienna . 2011.

11. Moës N, Dolbow J, Belytschko T. A finite element method for crack growth without remeshing. *International Journal for Numerical Methods in Engineering* 1999; 46(1): 131-150. doi: 10.1002/(SICI)1097-0207(19990910)46:1<131::AID-NME726>3.0.CO;2-J

12. Zi G, Belytschko T. New crack-tip elements for XFEM and applications to cohesive cracks. *International Journal for Numerical Methods in Engineering* 2003; 57(15): 2221-2240. doi: 10.1002/nme.849

13. Benvenuti E. A regularized XFEM framework for embedded cohesive interfaces. *Computer Methods in Applied Mechanics and Engineering* 2008; 197(49-50): 4367-4378. doi: 10.1016/j.cma.2008.05.012

14. Benvenuti E. An effective XFEM with equivalent eigenstrain for stress intensity factors of homogeneous plates. *Computer Methods in Applied Mechanics and Engineering* 2017; 321: 427-454. doi: 10.1016/j.cma.2017.04.005

15. Hettich T, Ramm E. Interface material failure modeled by the extended finite-element method and level sets. *Computer Methods in Applied Mechanics and Engineering* 2006; 195(37): 4753 - 4767. John H. Argyris Memorial Issue. Part Idoi: https://doi.org/10.1016/j.cma.2005.09.022

16. Parrinello F, Marannano G. Cohesive delamination and frictional contact on joining surface via XFEM. *AIMS Materials Science* 2018; 5(1): 127-144. doi: 10.3934/MATERSCI.2018.1.127

17. Oliver J, Huespe A, Sánchez P. A comparative study on finite elements for capturing strong discontinuities: E-FEM vs X-FEM. *Computer Methods in Applied Mechanics and Engineering* 2006; 195(37-40): 4732-4752.

18. Dugdale D. Yielding of Steel Sheets Containing Slits. *J. Mech. Phys. Solids.* 1960; 8: 100-104.

19. Barenblatt G. The mathematical theory of equilibrium cracks in brittle fracture. *Advances in Applied Mechanics* 1962; 7: 55-129.

20. Gdoutos E. *Fracture Mechanics. An introduction*. Kluver Academic Publishers . 1993.

21. Corigliano A, Allix O. Some aspects of interlaminar degradation in composites. *Comp. Meth. Appl. Mech. Eng.* 2000; 185(2-4): 203-224.

22. Spada A, Giambanco G, Rizzo P. Damage and plasticity at the interfaces in composite materials and structures. *Comp. Meth. Appl. Mech. Eng.* 2009; 198(49-52): 3884-3901.

23. Alfano G, Crisfield M. Finite element interface models for the delamination analysis of laminated composites: Mechanical and computational issues. *Int. J. Num. Meth. Eng.* 2001; 50(7): 1701-1736.

24. Parrinello F, Marannano G, Borino G. A thermodynamically consistent cohesive-frictional interface model for mixed mode delamination. *Engineering Fracture Mechanics* 2016; 153: 61-79. doi: 10.1016/j.engfracmech.2015.12.001

25. Parrinello F, Borino G. Non associative damage interface model for mixed mode delamination and frictional contact. *European Journal of Mechanics / A Solids* 2019; 76: 108-122.

26. Parrinello F, Failla B, Borino G. Cohesive-frictional interface constitutive model. *Int. J. Solids Structures* 2009; 46(13): 2680-2692.

27. Mosler J, Scheider I. A thermodynamically and variationally consistent class of damage-type cohesive models. *J. Mech. Physics Solids* 2011; 59(8): 1647-1668.

28. Guiamatsia I, Nguyen G. A thermodynamics-based cohesive model for interface debonding and friction. *Int. J. Solids Structures* 2014; 51(3-4): 647-659.

29. Serpieri R, Sacco E, Alfano G. A thermodynamically consistent derivation of a frictional-damage cohesive-zone model with different mode i and mode II fracture energies. *Eur. J. Mech., A/Solids* 2015; 49: 13-25.

30. Parrinello F, Borino G. Integration of finite displacement interface element in reference and current configurations. *Meccanica* 2018; 53(6): 1455-1468.

31. Simone A. Partition of unity-based discontinuous elements for interface phenomena: Computational issues. *Communications in Numerical Methods in Engineering* 2004; 20(6): 465-478. doi: 10.1002/cnm.688

32. Mergheim J, Kuhl E, Steinmann P. A hybrid discontinuous Galerkin/interface method for the computational modelling of failure. *Communications in Numerical Methods in Engineering* 2004; 20(7): 511-519. doi: 10.1002/cnm.689

33. Nitsche J. Über ein Variationsprinzip zur Lösung von Dirichlet-Problemen bei Verwendung von Teilräumen, die keinen Randbedingungen unterworfen sind. *Abhandlungen aus dem Mathematischen Seminar der Universität Hamburg* 1971; 36(1): 9–15. doi: 10.1007/bf02995904

34. Nguyen V, Nguyen C, Bordas S, Heidarpour A. Modelling interfacial cracking with non-matching cohesive interface elements. *Computational Mechanics* 2016; 58(5): 731-746. doi: 10.1007/s00466-016-1314-y

35. Truster TJ, Masud A. A Discontinuous/continuous Galerkin method for modeling of interphase damage in fibrous composite systems. *Computational Mechanics* 2013; 52(3): 499–514. doi: 10.1007/s00466-012-0827-2

36. Benedetti I, Aliabadi M. A three-dimensional cohesive-frictional grain-boundary micromechanical model for intergranular degradation and failure in polycrystalline materials. *Computer Methods in Applied Mechanics and Engineering* 2013; 265: 36-62. doi: 10.1016/j.cma.2013.05.023

37. Benedetti I, Gulizzi V, Milazzo A. Grain-boundary modelling of hydrogen assisted intergranular stress corrosion cracking. *Mechanics of Materials* 2018; 117: 137-151. doi: 10.1016/j.mechmat.2017.11.001

38. Versino D, Mourad HM, Dávila CG, Addessio FL. A thermodynamically consistent discontinuous Galerkin formulation for interface separation. *Composite Structures* 2015; 133: 595 - 606. doi: https://doi.org/10.1016/j.compstruct.2015.07.080

39. Lorentz E. A mixed interface finite element for cohesive zone models. *Computer Methods in Applied Mechanics and Engineering* 2008; 198(2): 302 - 317. doi: https://doi.org/10.1016/j.cma.2008.08.006

40. Noels L, Radovitzky R. An explicit discontinuous Galerkin method for non-linear solid dynamics: Formulation, parallel implementation and scalability properties. *International Journal for Numerical Methods in Engineering* 2008; 74(9): 1393-1420. doi: 10.1002/nme.2213

41. Radovitzky R, Seagraves A, Tupek M, Noels L. A scalable 3D fracture and fragmentation algorithm based on a hybrid, discontinuous Galerkin, cohesive element method. *Computer Methods in Applied Mechanics and Engineering* 2011; 200(1-4): 326-344. doi: 10.1016/j.cma.2010.08.014

42. Nguyen V. Discontinuous Galerkin/extrinsic cohesive zone modeling: Implementation caveats and applications in computational fracture mechanics. *Engineering Fracture Mechanics* 2014; 128(C): 37-68. doi: 10.1016/j.engfracmech.2014.07.003

43. Papoulia KD. Non-differentiable energy minimization for cohesive fracture. *International Journal of Fracture* 2017; 204(2): 143–158. doi: 10.1007/s10704-016-0167-x

44. Hirmand M, Papoulia K. A continuation method for rigid-cohesive fracture in a discontinuous Galerkin finite element setting. *International Journal for Numerical Methods in Engineering* 2018; 115(5): 627-650. doi: 10.1002/nme.5819

45. Veubeke B. dF. *Stress Analysis*. Zienkiewicz OC, Holister GS (eds), Chapter 9. Wiley: London . 1965.

46. Almeida J.P.M. ddFJ. An alternative approach to the formulation of hybrid equilibrium finite elements. *Computers and Structures* 1991; 40: 1043 - 1047.

47. Pereira OJBA. Hybrid equilibrium hexahedral elements and super-elements.. *Commun. Numer. Meth. Engng* 2008; 24: 157 - 165.

48. De Moitinho Almeida J, Almeida Pereira O. A set of hybrid equilibrium finite element models for the analysis of three-dimensional solids. *International Journal for Numerical Methods in Engineering* 1996; 39(16): 2789-2802.

49. M. Kempeneers JD, Beckers P. Pure equilibrium tetrahedral finite elements for global error estimation by dual analysis. *Int. J. Numer. Meth. Engng* 2010; 81: 513 - 536.

50. Almeida J.P.M. dPO. A set of hybrid equilibrium finite element models for the analysis of threedimensional solids.. *International Journal for Numerical Methods in Engineering* 1996; 39: 2789 - 2802.

51. Pereira O.J.B.A. ME. Adaptive methods for hybrid equilibrium finite element models. *Computer Methods in Applied Mechanics and Engineering* 1999; 176: 19 - 39.

52. Parrinello F. Restraining approach for the spurious kinematic modes in hybrid equilibrium element. *Computational Mechanics* 2013; 52(4): 885-901. doi: 10.1007/s00466-013-0851-x

53. E.A.W. Maunder JMdA, Ramsay A. A general formulation of equilibrium macro-elements with control of spurious kinematic modes: the exorcism of an old curse. *International Journal For Numerical Methods In Engineering* 1996; 39: 3175 - 3194.

54. E.A.W. Maunder JMdA. Hybrid-equilibrium elements with control of spurious kinematic modes.. *Computer Assisted Mechanics and Engineering Sciences* 1997; 4: 587-605.

55. Wang L, Zhong H. A traction-based equilibrium finite element free from spurious kinematic modes for linear elasticity problems. *International Journal for Numerical Methods in Engineering* 2014; 99(10): 763-788. doi: 10.1002/nme.4701

56. Zienkiewicz O, Taylor . *The Finite Element Method. 5th Edition*. Butterworth-Heinemann Press . 2000.

57. Parrinello F. Analytical solution of the 4ENF test with interlaminar frictional effects and evaluation of Mode II delamination toughness. *Journal of Engineering Mechanics* 2018; 144(4). doi: 10.1061/(ASCE)EM.1943-7889.0001433

58. Kobayashi A, Hawkins N, Barker D, Liaw B. FRACTURE PROCESS ZONE OF CONCRETE. In: No. 94. ; 1985: 25-50.

59. Rots J. *Computational Modeling of Concrete Fractures*. Delft University of Technology . 1988.

60. Oliver J, Huespe A, Pulido M, Chaves E. From continuum mechanics to fracture mechanics: The strong discontinuity approach. *Engineering Fracture Mechanics* 2001; 69(2): 113-136.

61. Gálvez J, Elices M, Guinea G, Planas J. Mixed mode fracture of concrete under proportional and nonproportional loading. *International Journal of Fracture* 1998; 94(3): 267-284. doi: 10.1023/A:1007578814070

62. Areias P, Belytschko T. Analysis of three-dimensional crack initiation and propagation using the extended finite element method. *International Journal for Numerical Methods in Engineering* 2005; 63(5): 760-788. doi: 10.1002/nme.1305